Faculty of Science

Evaluating DInSAR for measuring seasonal elevation dynamics at the Vissátvuopmi palsa mire complex in Northern Sweden

André Farjami

Degree of Master of Science (120 credits)
with a major in Earth Sciences
60 hec

Department of Earth Sciences
University of Gothenburg
2022 B1205

UNIVERSITY OF GOTHENBURG

UNIVERSITY OF GOTHENBURG
Department of Earth Sciences
Geovetarcentrum/Earth Science Centre

Evaluating DInSAR for measuring seasonal elevation dynamics at the Vissátvuopmi palsa mire complex in Northern Sweden

André Farjami

ISSN 1400-3821

B1205
Master of Science (120 credits) thesis
Göteborg 2022

Mailing address
Geovetarcentrum
S 405 30 Göteborg

Address
Geovetarcentrum
Guldhedsgatan 5A

Telephone
031-786 19 56

Geovetarcentrum
Göteborg University
S-405 30 Göteborg
SWEDEN

Abstract

During recent years the palsa mires of Fennoscandia have reported to be undergoing extensive lateral degradation, and in a warming environment the palsa mires of Sweden among others are threatened to thaw completely by the end of this century. Since subarctic peatlands account for 30% of the global soil organic carbon storage, small degradation changes in these areas globally, can potentially change the greenhouse gas emissions on a worldwide scale. Therefore it is important to predict future changes in these peatlands. The aim of this thesis was to evaluate use of Sentinel-1 data and the DInSAR method to create a Digital Elevation Model (DEM) and to quantify seasonal displacement dynamics over individual palsas in the Vissátvuopmi palsa mire in northern Sweden. The results showed that creation of a DEM was not possible over the area. The seasonal displacement dynamics over the two individual palsas in this study varied from a minimum of -0.03 cm to a maximum of 3.30 cm over the snow-free months for each of the years from 2019 to 2021. There were no consistent patterns in seasonal displacement dynamics, mainly due to the high variation between the displacements values observed. When analyzed in relation to temperature and precipitation, the best relationship with displacement was with mean temperature ($R^2 = 0.5238$), and showed a negative trend. SAR data are highly sensitive to precipitation and snow, which limits the useful data to only two and a half months per year (from July to mid-September) in a best case scenario. It was difficult to use the DInSAR method for the initial purpose of this thesis, however, other analysis approaches (e.g. ISBAS method) with InSAR data may be useful in future studies. For a more detailed investigation of palsa elevation changes and degradation, I would suggest other higher spatial resolution data instead, such as DEMs created from drone imagery data.

Table of Contents

List of Abbreviations

AOI	Area Of Interest
DEM	Digital Elevation Model
DInSAR	Differential Interferometry of Synthetic Aperture Radar
ESA	European Space Agency
ESD	Enhanced Spectral Diversity
ISBAS	Intermittent Small BAseline Subset
IW	Interferometric Wide Swath mode
RGB	Red-Green-Blue (color spectrum)
RTK-GPS	Real Time Kinematic Global Position System
SAR	Synthetic Aperture Radar
SBAS	Small BAseline Subset
SNAP	SeNtinel Application Platform
SMHI	Swedish Meteorological and Hydrological Institute
InSAR	Interferometric Synthetic Aperature Radar
ISBAS	Intermittent Small BAseline Subset

1. Introduction

The Fennoscandia palsa mires have been reported for a relatively long time (some palsas had already disappeared in the 1960s or even before that) to be undergoing extensive lateral palsa degradation (i.e. degradation caused by permafrost thaw), with very few signs of any new formation of palsa mires occurring during the past decades (Luoto & Seppälä, 2003; Sollid & Sørbel, 1998; Zuidhoff & Kolstrup, 2000). As pointed out by Borge et al. (2017) the rate of the lateral decay is also accelerating quickly and is speculated to continue in a warming climate, which in a worst case scenario could lead to a complete palsa mire loss in Fennoscandia by the end of the century (Fronzek, 2013). Therefore it is of utmost importance to predict future changes in these environments.

1.1. Aim

The aim of this thesis is to evaluate the potential of using DInSAR data derived from Sentinel-1 data as a tool for describing seasonal elevation dynamics over individual palsas within the Vissátvuopmi palsa mire complex located in northern Sweden. The research questions are, the following.

- What seasonal elevation dynamics can be revealed using DInSAR data from the snow-free months over individual palsas in the Vissátvuopmi palsa mire complex?
- What is the relationship between elevation changes in individual palsas as seen from DInSAR data and meteorological factors?
- Can a single DEM derived from DInSAR data be used to accurately measure elevation over individual palsas in the Vissátvuopmi palsa mire complex?

1.2. Background information

1.2.1. What is SAR, and InSAR?

Synthetic Aperture Radar (SAR) is an active imaging system using microwaves (Ferretti et al., 2007a), instead of a passive optical imaging system (e.g. optical satellite images or orthophotos). The main advantage over traditional imaging systems is that SAR has the ability to penetrate any cloud cover present at the time of image acquisition, due to its usage of microwaves. The SAR imaging systems can also operate both at night and day, since it uses an active transmission of microwaves (Feretti et al., 2007a) and works independent of any light source.

The SAR system also has an interferometric configuration, called *Interferometric Synthetic*

Aperture Radar (InSAR). InSAR allows for accurate measurements of the radiation travel path, due to its good coherence. The travel path variation measurements in combination with satellite position and time of image acquisition can be processed to generate a *Digital Elevation Model* (DEM), which can measure surface deformations of the Earth's surface with centimetric accuracy (Ferretti et al., 2007a).

A SAR image contains a measurement of the magnitude of radiation backscattered toward the radar by the objects in each SAR resolution cell. The measured backscatter is dependent more on the roughness of the scatterers on the terrain rather than the chemical composition. Usually rock walls and urban areas (infrastructure) show strong magnitudes, while open water basins and other smooth flat surfaces in general show low magnitudes of backscatter. The SAR image is usually visualized using a grey scale, with values ranging from 0 to 1; where bright pixels (closer to 1) indicate areas of strong backscattered radiation (e.g. urban infrastructure) and dark pixels indicate low amounts of backscattered radiation (e.g. smooth open water) (Ferretti et al., 2007a). Shown are two examples of a SAR interferogram with high overall coherence (Figure 1) and low overall coherence (Figure 2).

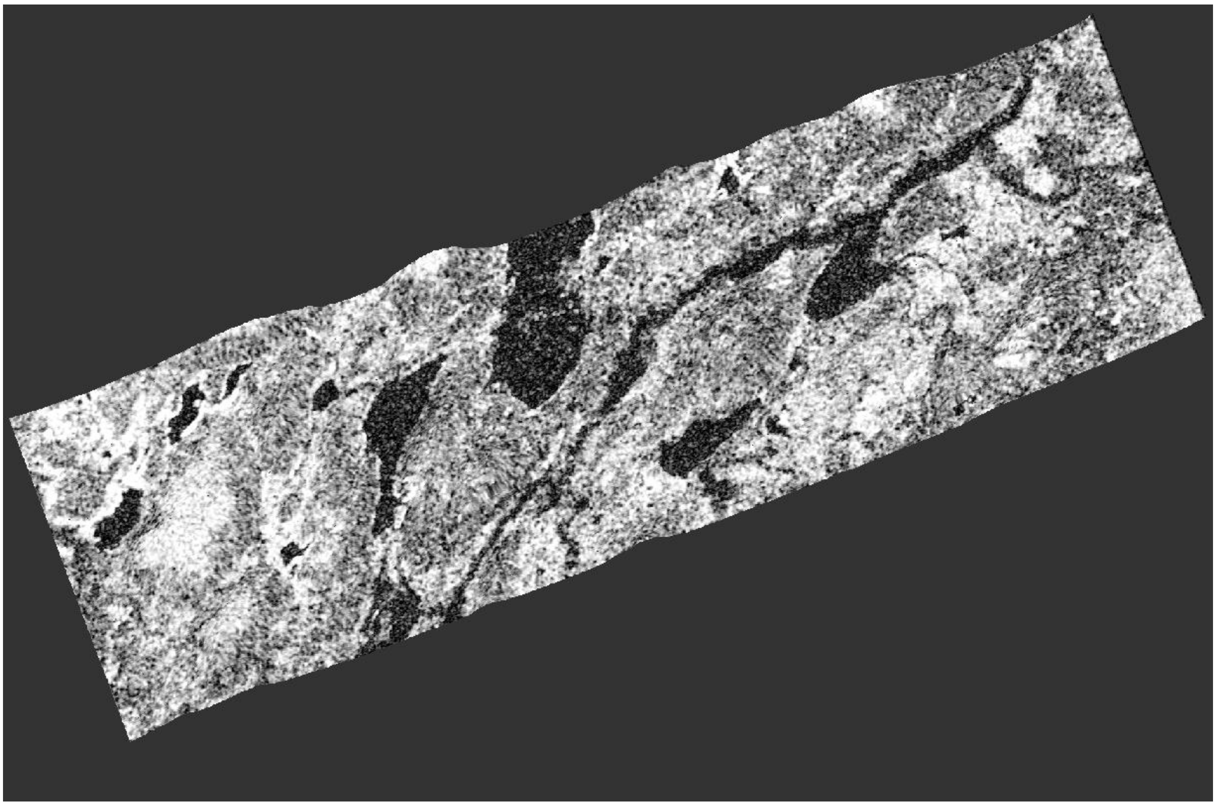

Figure 1: An example of a SAR interferogram with high coherence. Notice how well one can distinguish land areas (high backscatter – bright areas) from water (low backscatter – dark areas). This is the coherence for the interferogram from the 30th of June to 5th of August 2021, which had the highest measured coherence out of all interferograms used in this thesis.

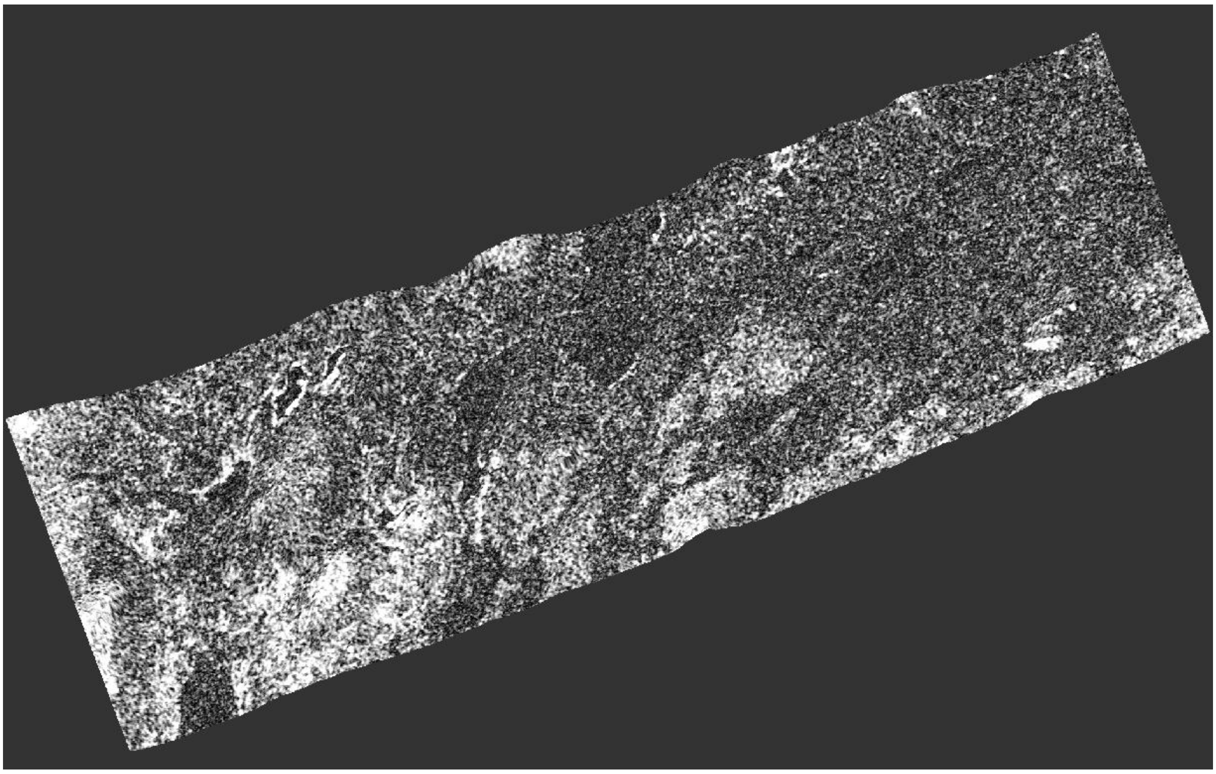

Figure 2: An example of a SAR interferogram with low coherence. Notice how difficult it is to distinguish land areas for water in a SAR image with low coherence. This is the coherence for the interferogram from the 11th of June to the 4th of August 2020, which had the lowest measured coherence out of all the interferograms used in this thesis.

However there is a major drawback in InSAR analysis, which is the decorrelation between the images due to changes of the surface properties, such as snow presence, soil moisture, or vegetational changes (Westermann et al., 2015; Zwieback et al., 2016). As pointed out by Westermann et al. (2015) when doing permafrost assessments SAR and optical image matching are highly complementary to each other. In circumstances where SAR fails (e.g. during wintertime) optical satellite imagery may work better and vice versa.

Another drawback of InSAR analysis is the need for images that have good temporal and perpendicular baselines to obtain good coherence within an interferogram. A SAR interferogram is a coregistration between two different SAR images, and is generated by cross-multiplying the pixel by pixel value of the first older SAR image with the newer second SAR image. This process is described more thoroughly by Bamler and Hartl (1998), Massonnet and Feigl (1998), and Rosen et al. (2000).

The temporal baseline is the number of days between the different acquisitions of the SAR images (which could be as low as 6 days under best weather conditions for Sentinel-1 data); the closer this gap is the higher the coherence of the interferogram will be, as demonstrated by Braun (2021). Coherence is the cross-correlation coefficient of the SAR image pair estimated over a small window, comprising only a few pixels. The coherence map of the interferogram is then created by computing the absolute value of the coherence on a moving window (average) that covers the interferogram (Ferretti et al., 2007a).

The perpendicular baseline is the perpendicular distance (in meters) between the line of sight measurements (this projected line is commonly called the slant range) for the different satellite positions during respective image acquisition when compared to each other (Ferretti et al., 2007a). This is visually represented in Figure 3. Depending on what the purpose of your investigation is, e.g. displacement measurements or DEM creation, some perpendicular baseline distances should be avoided. Generally speaking an interferogram with a perpendicular baseline less than 30 meters should always be avoided, since these interferograms are almost useless because of their high sensitivity to both phase noise and atmospheric effects according to Ferretti et al. (2007b). An optimal perpendicular baseline ranging from 150 up to 300 meters is suggested, when creating InSAR derived DEMs. For displacement measurement purposes there is no optimal perpendicular baseline, however it is recommended to have as small of a baseline as possible, since smaller baselines lead to higher expected coherence (Ferretti et al., 2007b).

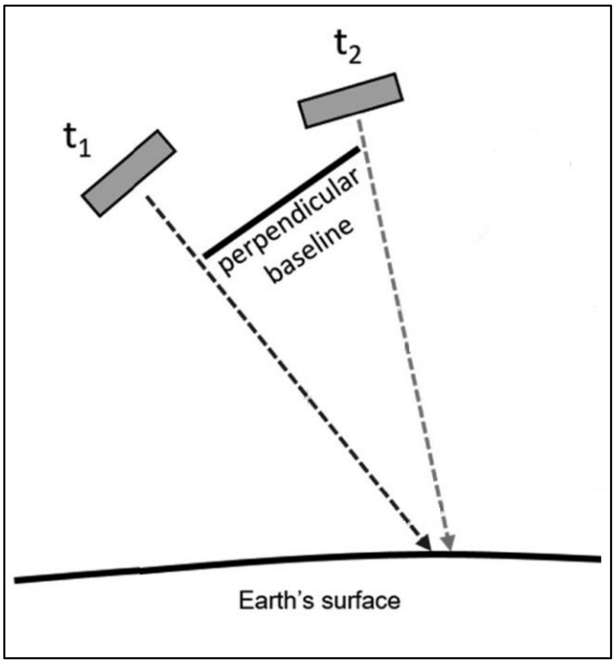

Figure 3 An image showing the perpendicular baseline between the first image acquisition (t_1) and the second image acquisition (t_2). The arrows are the satellites line of sight (slant range). Source: © Braun (2021).

1.2.2. What is DInSAR, SBAS and ISBAS?

There are many different methods that can be applied if one wants to use InSAR data. In the following, some common methods are described.

Differential Interferometry of Synthetic Aperture Radar (DInSAR) can be used to create high-precision surface displacement maps by converting phase differences of SAR backscattered signals during two different acquisition dates to line of sight displacement along the vector connecting the ground to the sensor (Gabriel et al., 1989). Therefore the displacement, however more SAR images can be used.

More sophisticated methods than DInSAR are the *Small BAseline Subset* (SBAS) and the closely related *Intermittent Small BAseline Subset* (ISBAS). The SBAS method is based on a combination of differential interferograms consisting of data pairs (SAR images) with a small orbital baseline (distance between the different satellites during image acquisitions) in order to prevent the spatial decorrelation phenomenon (Berardino et al., 2002). The major problem with the SBAS method is that it requires images with relatively high coherence, limiting the areas where the method can be applied to rocky or urbanized areas (Sowter et al., 2013). The ISBAS method was therefore developed by Sowter et al. (2013) to adapt the original SBAS method to use the intermittent coherence of areas in order to increase the number and point measurements distribution of land deformation. This significantly improves the capability to examine rural and vegetated regions, since SAR imagery over these regions usually exhibits lower coherence compared to urbanized areas. The usage of intermittent coherence by the ISBAS method has been demonstrated by Cigna and Sowter (2017) to increase the coverage of point measurements by 4 to 26 times more on average. The spatial coverage of ground motion solutions also increased from merely 4-12% for land pixels with SBAS method, to 39-99% with the ISBAS method for the investigated areas.

During this project the DInSAR method was used, mainly because the ISBAS method only came to light later in the project, but also DInSAR is easier to use and requires less processing than the other methods.

1.2.3. Common SAR bandwidths and satellites

The different SAR satellite sensors in orbit use different wavelengths and frequencies in their respective microwave bands. The most common bands are X-, C-, S-, L-, and P-band sensors.

The X-band sensor uses a frequency in the range between 8 to 12 GHz and wavelengths from 2.4 to 3.8 cm and is considered a high-resolution SAR sensor. The X-band sensor is typically used for urban and infrastructure monitoring or ice and snow monitoring, however it has little penetration into vegetation cover and thus fast coherence loss in vegetated areas, and are therefore not suitable in e.g. forest monitoring. The C-band sensor uses a frequency in the range between 4 to 8 GHz and wavelengths from 3.8 to 7.5 cm. C-band sensors are considered the SAR workhorse and it is the most commonly used microwave band. The C-band sensor is used in global mapping, displacement detection (e.g. after landslides or volcanic eruptions), and monitoring areas of low to moderate vegetation. The C-band sensor has improved penetration of vegetation cover when compared to the X-band sensor, and therefore also higher coherence over vegetated areas. The S-band sensor uses a frequency in the range between 2 to 4 GHz and wavelengths from 7.5 to 15 cm. The use of the S-band in the past was limited but is estimated to increase in the near future with newer S-band sensor satellites becoming available. The S-band sensor will be used in e.g. agriculture monitoring, and expands the C-band sensor applications for areas with higher vegetation density. The L-band sensor uses a frequency between 1 to 2 GHz and wavelengths from 15 to 30 cm and is considered a medium resolution SAR sensor. The L-band sensor is commonly used for Geophysical monitoring, biomass and vegetation mapping. Compared to the X-, C-, and S-band sensors the L-band has higher vegetation cover penetration. The P-band uses a frequency between 0.3 to 1 GHz and wavelengths from 30 to 100 cm and is considered an experimental SAR sensor. The P-band sensors is a relatively new addition to the SAR band sensor family with the first P-band sensor planning to be launched in 2023, the P-band will be used for biomass and vegetation mapping (Meyer, 2019).

Some of the common satellites using these different sensors are but not limited to; TerraSAR-X and TanDEM-X (X-band), ERS (1&2), Radarsat (1&2) and Sentinel-1 (C-band), NISAR (L-band), and BIOMASS (P-band). During this project Sentinel-1 data was used, mainly since it is free, widely available and has high temporal resolution.

1.2.4. What is an RTK-GPS?

To measure the elevation reference points on the palsas during the field trip a *Real Time Kinematic Global Position System* (RTK-GPS) was used. When using a RTK-GPS a *Global Navigation Satellite System* (GNSS) receiver is needed as well as a data link for transferring measuring data between the different devices in real time (Lantmäteriet, n.d.).

The simplest way to perform a RTK-measurement is to use two RTK-devices, one stationary reference station fixed at a known position (usually called the base station) and another device working as a moving receiver (usually called the rover) for measuring the different control points. With the help of the relative positioning, the rover combines its own GNSS-observations with the reference station, which reduces the sources of error and there after obtains the “exact” positioning. However this requires that both the reference station and the rover are observing the same set-up of GNSS-satellites, as well as the transfer of position and observation from the reference station to the rover provided by the data link occur in time (Lantmäteriet, n.d.).

1.2.5. Palsa description and elevation dynamics

Palsas are peat-covered mounds that can reach up to several meters in height, consisting of permafrost and mineral soil cores under a layer of peat. Since the peat exhibits good insulating potential, these permafrost landforms can survive in climates with mean annual temperatures just below the freezing point of water (0°C). Palsas are a permafrost phenomenon primarily found in regions with discontinuous or sporadic permafrost (Sollid & Sørbel, 1998). Sporadic permafrost regions are areas in which the amount of frozen ground ranges between 10 to 50% (Brown et al., 2002). In these sporadic permafrost regions, the ground temperature of the permafrost is usually close to the water freezing point, and as a consequence even small increments in air temperature can result in permafrost thawing (Sjöberg et al., 2015). Additionally, the permafrost distribution and thawing in permafrost peatlands are influenced by more than just climatic changes, such as hydrological, geological, morphological, and erosional processes that usually coexists in complex interactions. As an example, the groundwater flow in permafrost regions can accelerate thaw driven by global warming and change thaw patterns (McKenzie & Voss, 2013), and erosional processes leading to palsa degradation could be e.g. block erosion, thermokarst and wind erosion (Zuidhoff, 2002). Because of these complex interactions, permafrost peatlands usually exhibit dynamic thermal structure and extent, as the distribution of permafrost landforms (e.g. dome- and ridge-shaped palsas) varies with climatic and local conditions (Sjöberg et al., 2015).

Permafrost peatlands store large amounts of soil organic carbon, where the subarctic peatlands accounts for more than 30% of the global soil organic carbon storage according to Hugelius et al. (2014). The dynamic nature and spatial extent of these peatlands creates potential implications across the pan-Arctic according to Hugelius et al. (2014) and Tarnocai et al. (2009). As pointed out by Sjöberg et al. (2015), the combination of the large amounts of organic soil carbon stored and the high potential of permafrost thawing makes these permafrost peatlands geochemical hotspots in the warming Arctic. Since thawing of the permafrost peatlands can potentially lead to large pools of soil organic carbon that have previously been protected from mineralization by sub-zero temperatures could start mineralizing. This mineralization could then lead to higher greenhouse gas fluxes with the atmosphere, creating a positive feedback (Schuur et al., 2015; Yang et al., 2010), which further accelerates global warming in return. Direct observations of permafrost degradation made by Plaza et al. (2019) showed a high annual carbon loss of over 5%/year, which indicates that some permafrost regions can undergo a relatively fast degradation process, within a short time span. Therefore it is important to start investigating these areas, before they may disappear completely.

As pointed out by Olvmo et al. (2020) deeper understanding of the different climatic drivers effect on palsa degradation is insufficient today, however in some permafrost peatland studies the authors considers the ongoing palsa degradation to be driven by the increasing trend in both air temperature and precipitation (e.g. Sannel et al., 2016; Zuidhoff & Kolstrup, 2000). Rudy et al. (2018) also suggests that surface displacements in permafrost regions are influenced by different vegetation types, soil material, micro topography and soil moisture in addition to the ground ice content. In northern Sweden there are already some permafrost areas that have had rapid degradation due to short-term climatic events (e.g. Johansson et al., 2011; Åkerman & Johansson, 2008). There is also some documentation that the sporadic permafrost regions of Sweden exhibit increased thaw depth and active permafrost layer (i.e. a greater extent of the permafrost zone underneath the peat cover is thawing) (e.g. Johansson et al., 2011; Sannel et al., 2016; Åkerman & Johansson, 2008).

1.2.6. The Vissátvuopmi palsa mire complex

The dome- and ridge-shaped palsas that have been examined in this study are part of the Vissátvuopmi palsa mire complex (N 68°47′50″, E 21°11′30″), which is the largest coherent palsa mire complex in Sweden (Olvmo et al., 2020). The Vissátvuopmi palsa mire complex also accounts for around 14% of Sweden’s total amount of palsa classified regions according to Backe (2014).

There are three different types of palsa morphologies present in the study area, plateau, dome-shaped, and ridge-shaped palsas. Here are a short description of each of the different types. Plateau palsas are flat and relatively massive palsas that can extend anywhere between tens of meters to several hundreds of meters in diameter. Plateaus palsas are rarely elevated more than 2 meters over the surrounding bog (Sollid & Sørbel, 1998). Dome-shaped palsas are relatively small palsas and usually isolated from other palsas, and they can have a diameter ranging from a few meters up to tens of meters and a height of a couple of meters (Sollid & Sørbel, 1998). As the name suggests these palsa morphologies looks like small domes or dunes. Ridge-shaped palsas are also isolated palsa morphologies. They can have a considerable elevation when compared to the surrounding environment. These palsa morphologies are more elongated than the dome palsas and have the shape of a miniature mountain ridge. The characteristics of palsas are dependent on local factors, therefore it is difficult to draw any general conclusions what is considered a normal palsa characteristics on a global scale. In Sweden palsas can range from a couple of decimeters up to 7 meters in height according to Backe (2014).

The dominating palsa morphology of the Vissátvuopmi complex, is the plateau palsas, which have decreased in area drastically between 1955 to 2016 with a 30% lateral loss (from 69.5 hectare to 48.8 hectare) and an average annual degradation rate of -0.58%/year. However the average annual degradation rate has varied over the years, with the lowest rate of -0.29%/year from 1963 to 1983, and the highest rate of -0.88%/year from 1994 to 2010. The average annual degradation rate is still relatively high after 2010, with an annual rate of -0.83%/year during 2010 to 2016. This means that the average annual degradation rate has doubled from 1994 to 2016, when compared to the average annual degradation rate from 1955 to 1994. These results from Olvmo et al. (2020) are similar to previous studies from other parts of Fennoscandia, e.g. Laivadalen in northern Sweden (Zuidhoff & Kolstrup, 2000), Finnish Lapland in northern Finland (Luoto & Seppälä, 2003), Finnmark in northern Norway (Borge et al., 2017), and Dovrefjell in southern Norway (Sollid & Sørbel, 1998), indicating extensive and varying palsa degradation rates over much of Fennoscandia.

The dome- and ridge-shaped palsas have undergone a higher degradation rate than the dominating plateau palsas in the region, which a similar study has also showed from Norway (Borge et al., 2017). Over 35% of the dome-shaped palsa and 54% of the ridge-shaped palsa have degraded from 1955 to 2016, with annual degradation rates of -0.71%/year (dome) and -1.25%/year (ridge). According to Olvmo et al. (2020) this shows that palsa morphology effects the trend of the palsa degradation rate. They point out that the height of the palsa could affect the degradation rate as taller palsas (e.g. ridge palsas) can accumulate more snow on the leeward side due to snow drift, compared to shorter palsas (e.g. plateaus palsas and dome palsas). If the snow depth were to be thicker, the cold penetration effect would also be lower in the winter and additionally more meltwater would be available during the spring and summer months, leading to an increased permafrost thawing and peat block erosion at a local scale. Another factor could also be that taller palsas could be exposed to stronger winds and therefore also a stronger abrasion of the peat layer as pointed out by Seppälä (2003). The combination of these factors could lead to a loss of the insulating effect the peat has on the underlying permafrost during the summer months as pointed out by Olvmo et al. (2020). However they also point out that more research is needed to fully understand the relationship between palsa degradation rates and palsa morphology.

1.2.7. Climatic conditions required for palsa formation in the study area

Climate data analysis over Vissátvuopmi comes from Olvmo et al. (2020) study in which they have used height compensated climate data from two nearby meteorological stations from

SMHI located in Karesuando (station numbers 192830/192840) and Naimakka (station numbers 19190/191910). For Vissátvuopmi, Olvmo et al. (2020) calculated that the "equilibrium points" for the annual air temperature and precipitation are estimated to be -4.0 ℃ and 363 mm respectively. The equilibrium point is the value of a climatic driver, in which the annual freezing and thawing of the palsa is considered to be in balance (i.e. the annual palsa degradation rate is zero).

Over the last 30-year period of their study (1987-2016) the average annual air temperature was -2.1 ℃ and annual precipitation was 481 mm (an anomaly of ±1.9 ℃ and 118 mm respectively). All the climatic variables they examined except for the number of frost days showed large anomalies at the end of the study period when compared to calculated equilibrium points. This implies that disadvantageous climate conditions for palsa formation are present in the study area.

In fact, the average annual air temperature conditions in the study area have been unfavorable for palsa formation for more than a century, and since the 1940s precipitation conditions have also been unfavorable. Today there no longer exists any climatic conditions that would favor new palsa formation in the study area. According to Olvmo et al. (2020) if the annual decay rates continue at the same rate as the last two decades (-0.9%/year), about half of the Vissátvuopmi palsa mire complex may disappear by the end of this century. Since smaller palsas are more sensitive to the enhanced downward heat flux than larger palsas, this suggests that the lateral degradation rate is expected to increase as the palsas shrinks in size with time. Therefore it is most likely that the decay rates in the future will become higher than today's rate due to the combination of increased temperature, precipitation, and the palsa mires geomorphology and size. Even higher decay rates have been observed in other permafrost peatland regions (e.g. Borge et al., 2017; Mamet et al., 2017), probably because palsa mires in these areas are generally smaller than the palsa mires at the Vissátvuopmi palsa mire complex.

As pointed out by Olvmo et al. (2020) a shift in the heat balance towards a warmer, longer and more moist thawing season has occurred, which enhances the downward heat flux and thawing of permafrost. The winter has also become warmer and moister, leading to more snowfall and deeper snow depths, which enhances the snow cover insulation and decreased freezing potential. The impact of increased precipitation in the form of snow is uncertain, due to differences in snow drift and in number of days below zero between the study area and Karesuando (Olvmo et al., 2020).

2. Study area and material

2.1. Data

2.1.1. Meteorological data

The meteorological data used in the project was provided by *Swedish Meteorological and Hydrological Institute* (SMHI). The weather station data used is located in Naimakka (station number 191910), approximately 17.5 km from the dome palsa and 18.5 km from the ridge palsa. Air temperature and precipitation data from the Naimakka weather station was used in the project.

The mean, maximum and minimum air temperature data seen in the results section was height compensated to match theoretical air temperature at the palsa mires. The height compensation was done based on the conception that the air temperature drops 1°C per 100 meters of elevation change. Since the elevation difference between the palsas and the weather station were around 70 meters, the height compensated temperature was thought to be 0.7°C lower than the measured temperature at Naimakka weather station.

2.1.2. Sentinel-1 and DInSAR data

The DInSAR data created in this project was made from Sentinel-1 radar data, provided by European Space Agency (ESA) through their web platform Copernicus Open Access Hub, which is free for anyone. The Sentinel-1 mission is comprised of a constellation of two satellites, Sentinel-1A (launched into orbit the 3rd of April 2014) and Sentinel-1B (launched into orbit the 25th of April 2016), sharing the same orbital plane. The Sentinel-1 mission includes a C-band sensor (wavelength of $\approx$ 5.55 cm) operating in four different imaging modes with different resolutions and coverages. The mission also provides dual polarization capability for most of the imaging modes, short revisiting times (an orbital repeat cycle of only 12 days for each individual Sentinel-1 satellite and only 6 days for the constellation according to Meyer (2019)) and fast product delivery (ESA, n.d.). The different modes and their properties are summarized in Table 1.

Table 1: An overview of the different imaging modes of the Sentinel-1 mission, including the modes geometric resolution in meters, ground coverage in kilometers and their polarizations. The SM, IW and EW modes have dual polarization, while the WV mode only has singe polarization. All information is directly derived from ESA's own documentation.

Imaging mode	Geometric resolution (m)	Ground coverage (km)	Polarization
Strip Mode (SM)	5 × 5	375	HH + HV or VV + VH
Interferometric Wide Swath Mode (IW)	5 × 20	250	HH + HV or VV + VH
Extra Wide Swath Mode (EW)	20 × 40	400	HH + HV or VV + VH
Wave Mode (WV)	5 × 20	100	HH or VV

A total of 21 SAR images from Sentinel-1 Interferometric Wide Swath (IW) mode were downloaded from the dates of July to September between 2019 to 2021 (Table 2), and used to create a total of 17 interferograms, with 3 interferograms for 2019, 6 interferograms for 2020 and 8 interferograms for 2021. VV polarization was used for the SAR images. The VV polarization achieves higher coherence over vegetated areas than the other polarizations available.

More SAR images are available before 2019, however the number of useful images are only a few due to precipitation, as well as perpendicular and temporal baselines. Therefore I did not use SAR images older than 2019.

Table 2: An overview of the 21 SAR images used in the project, with their respective date of acquisition. All images are acquired around 1600 hours (4 pm). Temporal baseline: the number of days elapsed between the images. Perpendicular baseline: the perpendicular distance (in meters) between the line of sight positions for the different satellites when compared to each other. Air temperature: the temperature during the acquisition from the nearest weather station in Naimakka. Precipitation: the amount of precipitation during date of the acquisition (from 00:00 to 16:00) from measurements at the weather station in Naimakka.

Date of acquisition	**Temporal baseline (days)**	**Perpendicular baseline (m)**	**Air Temperature (°C)**
19/07/23	-	-	24.3
19/07/29	6	66.28	8.7
19/08/22	24	-83.90	13.3
19/08/28	6	120.10	23.1
19/09/03	6	-67.89	12.0
20/07/05	-	-	9.1
20/07/11	6	-126.00	11.7
20/08/04	24	90.11	14.5
20/08/10	6	-164.87	12.6
20/09/03	24	184.54	14.9
20/09/09	6	164.14	8.9
20/09/15	6	100.60	7.4
21/07/06	-	-	24.8

21/07/18	12	-112.50	12.4
21/07/24	6	119.25	13.1
21/07/30	6	-43.37	12.6
21/08/05	6	47.71	15.9
21/08/17	12	-53.89	13.5
21/08/23	6	72.14	9.7
21/08/29	6	-162.41	13.9
21/09/04	6	81.45	5.8

2.1.3. Other remote sensing data

Since rain and snow changes the amount of backscatter radiation of the radar beams, which in return lowers the coherence in the SAR images, using images acquired during snowy or rainy days should be avoided. To check that no rain occurred during the day of acquisition, precipitation data provided by SMHI from Naimakka weather station was used. To check if snow was present during the day of acquisition, satellite imagery from the Sentinel Hub Earth Observation Browser (EO Browser) was used. The EO Browser is a web access portal for satellite data from ESA’s Sentinel-1 & -2 programs, among others. Aerial photographs used with 0.5 m pixel size were taken during 2016 by The National Land Survey (sv. Lantmäteriet). The vegetation map used in the project was from the latest vegetation mapping (sv. Fjällvegetationskarta) also done by The National Land Survey in 2012.

2.2. Study area

2.2.1. Field trip

As part of the project a field trip to Saarikoski was conducted during the 8th to 15th of September (Figure 4). The main reason behind the field trip was to measure reference elevation points using a RTK-GPS, which should have worked as an accuracy assessment for the DEM derived from the DInSAR data. The number of measured reference points over the dome palsa were 381 and over the ridge palsa were 127 points. The points were taken with 5 meter spacing to match the resolution of the Sentinel-1 IW mode (5 m × 20 m).

2.2.2. Palsas of interest in the study area

The palsas of interest for this study were located in the Vissátvuopmi palsa mire complex (Figure 4). The dome palsa covers approximately 1.54 hectares, while the ridge palsa is smaller covering around 0.46 hectares.

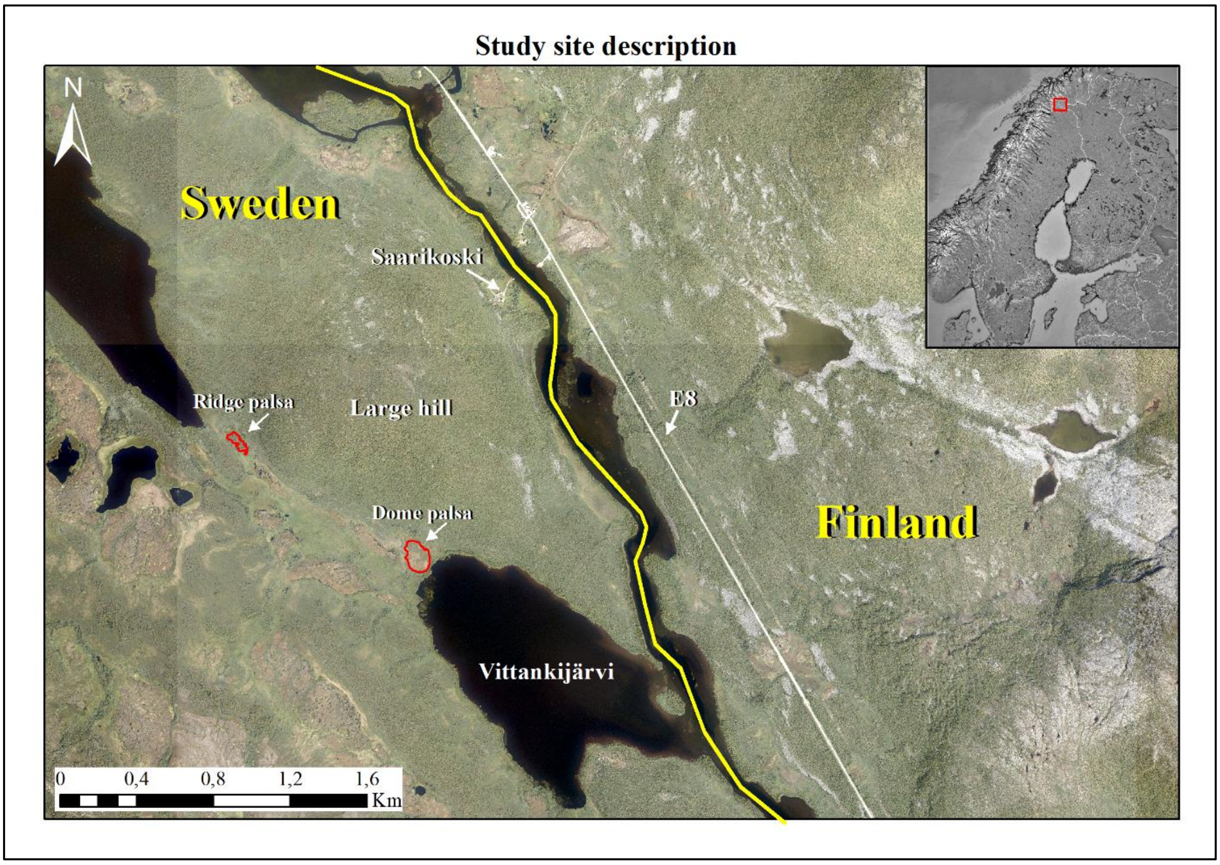

Figure 4: An overview of the study area, with the dome and ridge palsa mires outlined in red. During the field trip we stayed at the nearby settlement of Saarikoski, which is located near the border (yellow line) between Sweden and Finland. The closest road is the European road 8 (E8) located in Finland. Interesting landmarks in the study area were the relatively large lake Vittankijärvi and the relatively massive large hill, the influence of these landmarks on the displacement results are discussed in the discussion section. Photograph © Lantmäteriet (2016).

For analysis purposes, most of the *Area Of Interest* (AOI) on the dome and ridge palsas were located in erosion zones on respective palsa. Mainly because these areas are undergoing higher degrees of displacement when compared to the rest of the palsa, which were thought to produce better displacement estimation results.

AOIs on the dome palsa were located at the north end of the palsa (Figure 5). The first and second AOI were both degradation zones caused by block erosion located on the north western side of the dome palsa. Similarly the third AOI was also a degradation zone caused by block erosion on the north eastern side. The fourth AOI was an area that had undergone considerable vegetational change during recent years and is located on the north eastern side of the palsa. Similar to the first, second and third AOI, the fifth AOI is also a degradation zone caused by block erosion located on the north eastern side.

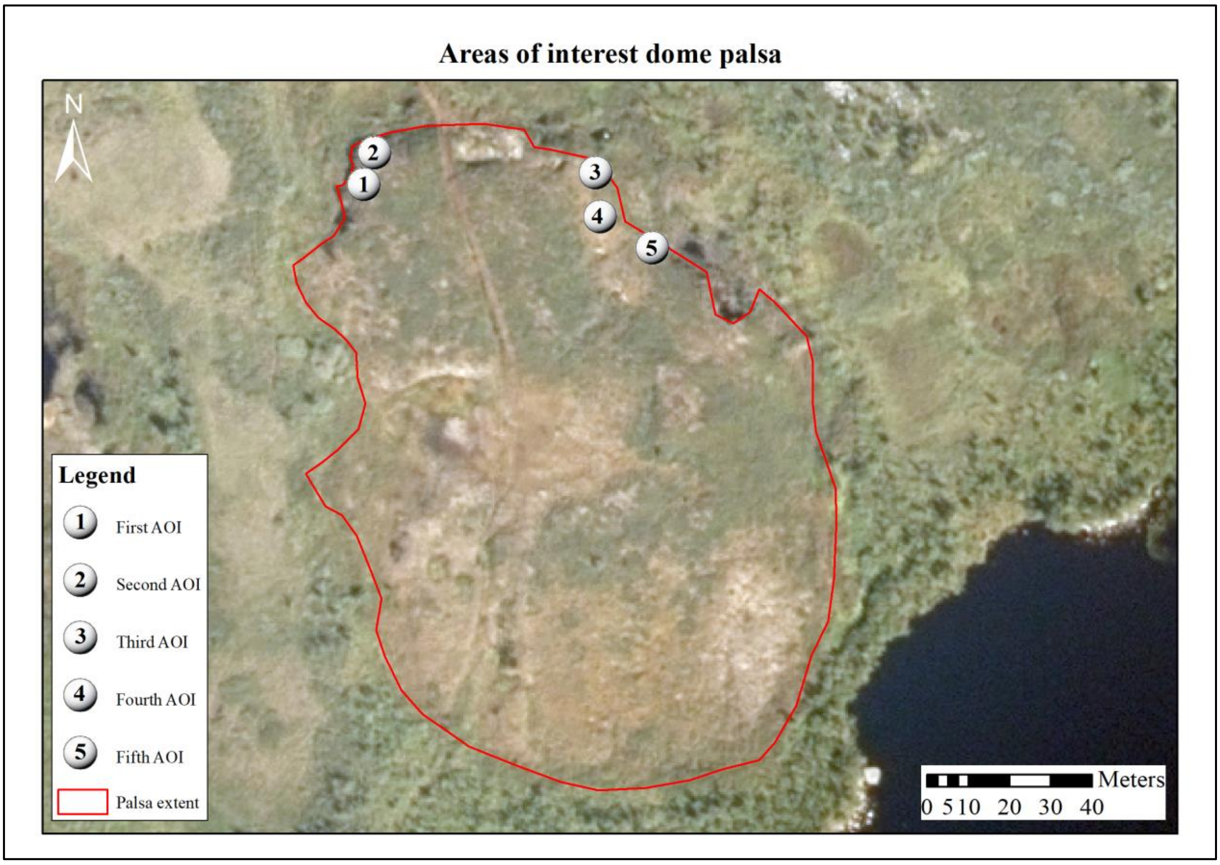

Figure 5: An overview of the Areas of Interest (AOIs) on the dome palsa. Photograph source: © Lantmäteriet (2016).

The AOIs on the ridge palsa are all located along the major degradation zone on the north to north east side (Figure 6). The first AOI is located the furthest north of the AOIs and the fifth AOI is located the furthest north east of the AOIs, the rest of the AOIs are located between the first and the fifth AOI. The degradation zone on this palsa is also caused by block erosion similar to the degradation zones at the dome palsa.

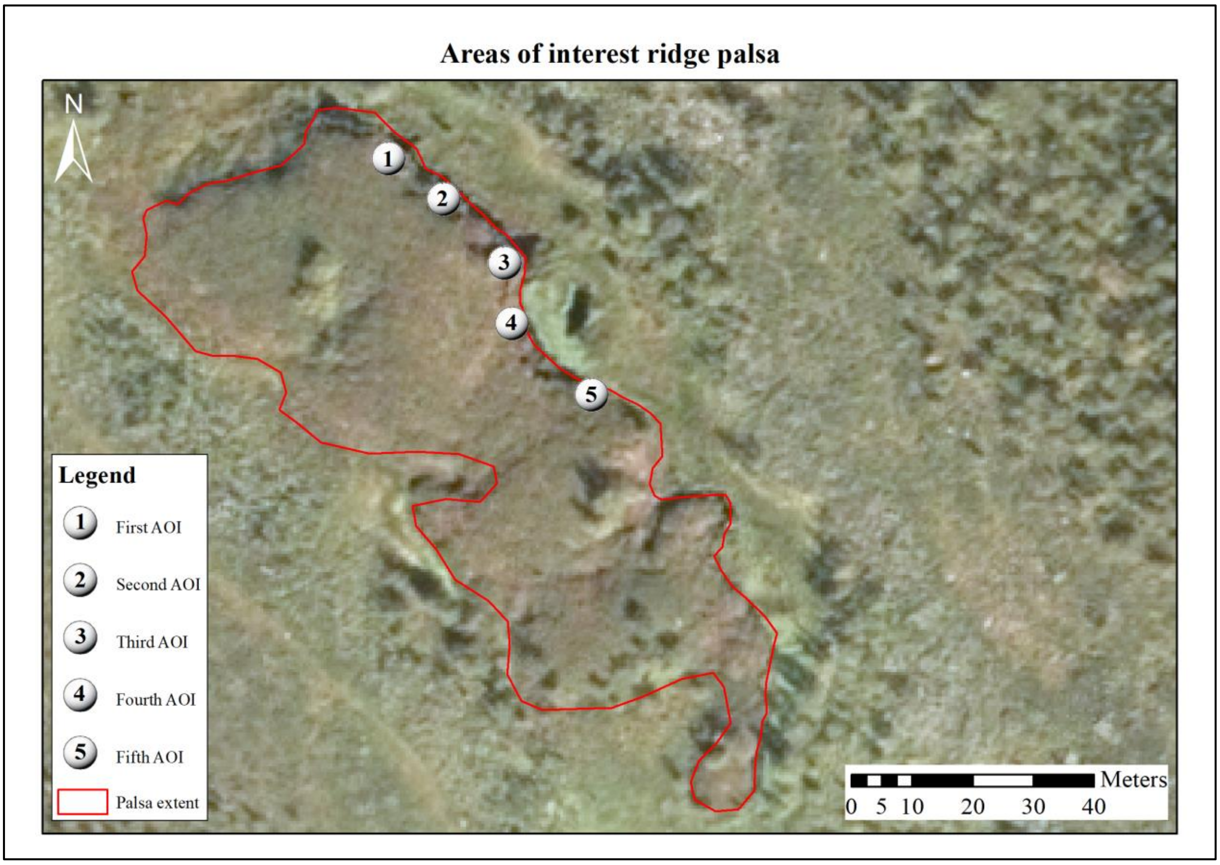

Figure 6: An overview of the Areas of Interest (AOIs) on the ridge palsa. Photograph source: © Lantmäteriet (2016).

2.2.3. The climate variation in the study area between during 2019 to 2021

The mean annual air temperature between 2019 to 2021 in the study area are all sub-zero, with the warmest of the three years being 2020 and the coldest being 2019 (Table 3). According to the annual precipitation from the weather station in Naimakka, the wettest season was 2020 and the driest season was 2019 (Table 3). All annual air temperatures were higher than the equilibrium point (-4.0 °C) suggested by Olvmo et al. (2020). However during the 2021 and 2019 seasons, the annual precipitation was actually lower than the equilibrium point (363 mm).

Table 3: A summary of the mean annual air temperature and annual precipitation in the study area from 2019 to 2021. The temperature data has been compensated for elevation differences between the weather station at Naimakka and the location of the study area. The annual precipitation is directly derived from measurements at the Naimakka weather station.

Year	**Mean annual air temperature (°C)**	**Annual precipitation (mm)**
2019	-2.7	349.4
2020	-0.9	501.8
2021	-2.6	355.5

2.2.4. Vegetation types in the study area

According to the latest vegetational mapping of the area by The National Land Survey (sv. Lantmäteriet) vegetation in the area mostly open bog vegetation, shrub heath, bog land deciduous forest and shrub covered mire (Figure 7). Both palsas investigated are located in open bog vegetation.

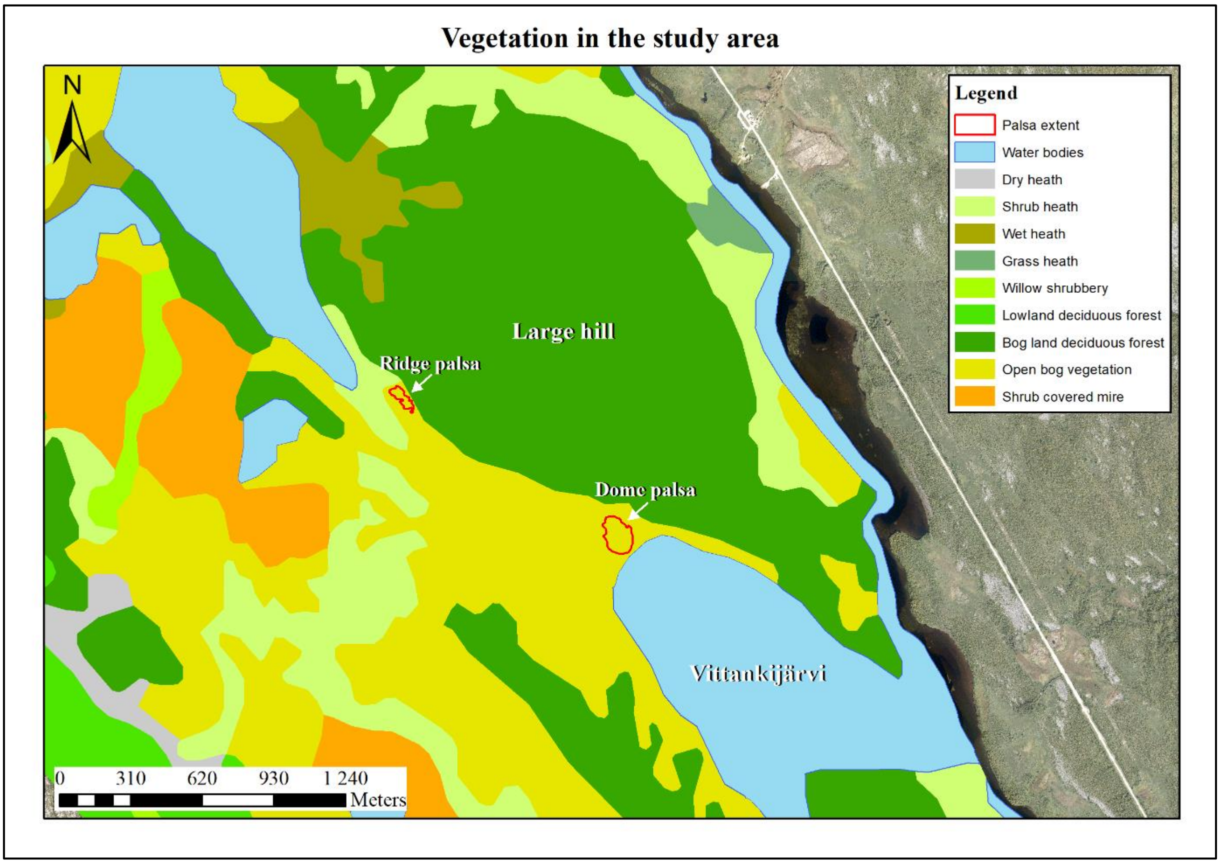

Figure 7: A vegetation map over the study area, indicating that most of the vegetation types in the area are open bog vegetation, shrub heath, bog land deciduous forest and shrub covered mire. The vegetational mapping was done in 2012 by The National Land Survey (sv. Lantmäteriet). Vegetation map source: © Lantmäteriet 2012.

3. Methods

3.1. DInSAR processing with SNAP

For the DInSAR data processing ESA’s SeNtinel Application Platform software (SNAP, version 8.0.9.) was used, since SNAP is especially developed to process satellite imagery from ESA’s different Sentinel satellite systems. The processing was done in pairs of two SAR images at a time, for example, images acquired by the 23rd to 29th of July 2019 was processed together and then the images acquired by the 29th of July to the 22nd of August 2019 was processed together (Table 2). This procedure was then repeated for the images throughout the year. The process was also repeated for images acquired during 2020 and 2021. The processing steps used were derived from Braun and Veci (2021), however some processing steps were modified, and the processing is described in the following text.

First, the image quality of the SAR images was checked before the processing began. The first processing step to derive DInSAR data was to coregister the two SAR images (the older image became the primary image and the newer image became the secondary image), and for this step I used the S-1 TOPS Coregistration with ESD (Enhanced Spectral Diversity) tool. The tool splits the original SAR image into smaller pieces, mainly to lower processing times; additionally the tool adds relevant orbital information (position of the satellite during the acquisition of the image) for each of the images. The tool also uses a DEM to the coregistrated images, which adds height data to the images. For this I used the Copernicus 30 meter Global DEM. The tool then performs Enhanced Spectral Diversity, which enhances the quality of the coregistrated images, by making small adjustments to the secondary image. All these steps can also be done individually as well, which can be necessary since this tool requires modest processing power, which a standard laptop may not achieve.

To analyze the data coregistration quality an RGB (Red-Green-Blue) representation test was used, which is mainly done to check if the two images are correctly aligned. In the RGB test the primary image (the older image) was assigned the colors red and green, while the secondary image was assigned the color blue. Therefore if parts of the image are dominated by the color yellow (red + green) these areas are dominated by the primary image, on the other hand if the areas are dominated by the color blue the area is dominated by the secondary image instead. If the coregistration is perfect over an area it is represented by the color white (red + green + blue). However usually the coregistration is not perfect even though it may be quite good in only very small parts of the whole SAR image. A bad coregistration is therefore an image that is either dominated by yellow or blue (Figure 8). However if the colors yellow, blue and white are randomly distributed over the area of interest (Figure 9), it is considered to be a good coregistration.

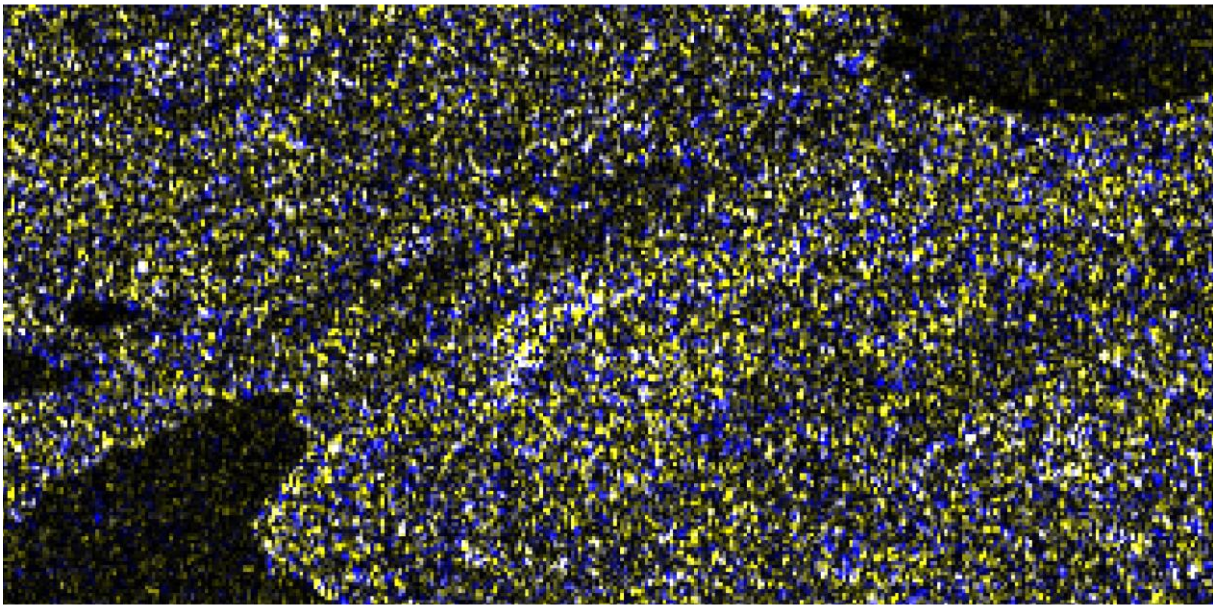

Figure 8: An example of an RGB-test were the coregistration is dominated by the primary image (yellow pixels). This is the RGB-test for the interferogram between the 23rd to 29th of July 2021.

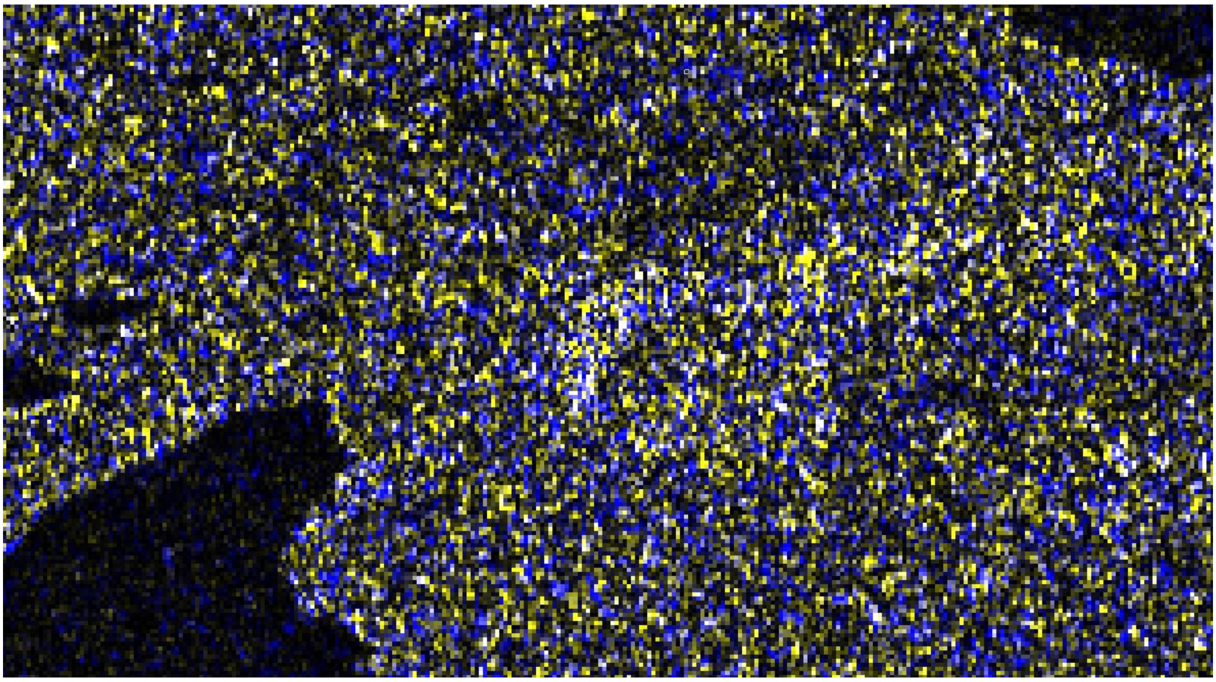

Figure 9: An example of an RGB-test were the coregistration is not dominated by neither the primary nor the secondary image. Also notice the amount of white pixels are higher in this RGB-test than the previous example (Figure 8). This is the RGB-test for the interferogram between the 6th to 18th of August 2021.

For the next step of the processing I used SNAP's GraphBuilder, which allow several tools in a sequence to be run by building up a logical graph (Figure 10), instead of running all tools individually. In GraphBuilder it was possible to first load the coregistered image from the previous processing step, and then to create the interferogram using the coregistered image. To avoid image overlapping after the interferogram formation, in the third step the TOPSAR-Deburst tool was used, as this tool removes parts of the two coregistered SAR images that overlap. In the fourth step the Goldstein phase filter was applied to the interferogram. The Goldstein phase filtering (Goldstein & Werner, 1998) reduces the amount of residue which improves the accuracy of "phase unwrapping" that is done in a later step, and explained in the following text. The last step of the graph basically just creates/writes an output file.

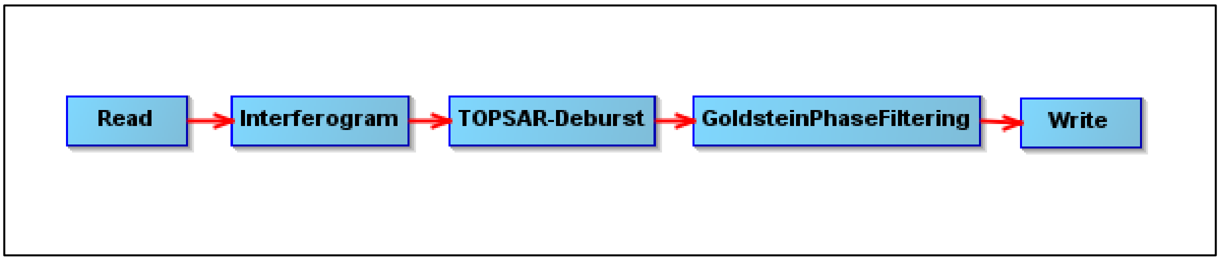

Figure 10: The processing graph compiled using GraphBuilder. In the first tab, the coregistered image from the first processing step were loaded. In the second tab, the interferogram were created. In the third tab, the interferogram were deburstеd. In the fourth tab the deburstеd interferogram were filtered. In the last tab the output file were created.

During the next step of the processing I created a subset of the filtered data from the previous step, since my study area covers only a small portion of the filtered data. This was done to reduce the amount of data being created in the coming steps.

The next step of the processing was the phase unwrapping and for this process I used the SNAP plugin program SNAPHU. Before the phase unwrapping could begin I needed to export the output file from the previous graph to SNAPHU, and this is done with the Snaphu Export tool. Then I began the phase unwrapping using the tool Snaphu-unwrapping. The SNAPHU phase unwrapping recovers definite phase data from a 2-D array of phase values and is an implementation of the Statistical-cost, Network-flow Algorithm for Phase Unwrapping (Chen & Zebker, 2000, 2001, 2002). Since SNAPHU is a plugin program, the data processed is not directly loaded into SNAP, but instead needs to be imported to SNAP, and done with the SNAPHU Import tool.

Conversion of the data from phase values to ground displacement values, was done with the Phase to Displacement tool. This tool converts the phase interferogram into a displacement raster. Since the displacement raster only contains displacement values, I created a new band in the displacement raster for the coherence. The coherence values are necessary later in the processing since these values will be used to mask out areas of low coherence. The coherence values will also be used evaluate the quality of the data later on.

Thereafter the displacement raster needed to be terrain corrected, using the tool Range-Doppler Terrain Correction. This tool removes distortions from the data due to factors such as, the satellite tilt during image acquisition (the sensor is side looking). The terrain corrections are intended to circumvent the different distortions so that the geometric representation of the imagery is as close as possible to reality. Additionally the tool also adds a DEM (I used Copernicus 30 meter DEM) and a reference system (I used SWEREF 99 TM, Sweden's national reference system).

The last part of the processing was to mask out areas of low coherence, since areas of low coherence usually have low data quality. There is no general value at which coherence is to be considered too low and masked out, but I chose to mask out areas that had a coherence value below 20%. Thereafter the masked and corrected displacement raster, for which there was one per image date pair, was further analyzed in ArcMap. The processed DInSAR data has a grid cell resolution of 10 m × 10 m, which is an upscaled version of the original Sentinel-1 IW modes resolution (5 m × 20 m).

3.2. ArcMap analysis

ArcMap (version, 10.8.1.) from Environmental Systems Research Institute (ESRI) was mainly used to interpret the displacement rasters that were created in SNAP and for creating the maps that have been used in the project (Figure 4, 5, 6 & 7). No heavier processing was done within ArcMap.

3.3. DInSAR displacement, relationship statistics and coherence values

3.3.1. DInSAR displacement

The DInSAR displacement result presented in the following results section (section 4.1.) was derived from the mean displacement in pairs of two DInSAR interferograms. For example, the displacement results from the first period during the 2019 season (from the 23rd of July to the 22nd of August) are mean displacement values of the interferograms between the 23rd to the 29th of July and the 29th of July to the 22nd of August. This procedure was then repeated for the rest of the interferograms for each respective season.

3.3.2. Relationships between displacement and meteorological conditions

To investigate if there existed any relationship between meteorological conditions (e.g. the mean, maximum and minimum air temperature and total precipitation) and the displacement trends, linear regressions were calculated. The linear regressions were done based on displacement values over the whole investigated period (2019 to 2021) for each of the palsa types. The relationships and their respective coefficient of determination (R^2) can be seen in the results section (section 4.2.).

3.3.3. Coherence values description

To test the quality of the DInSAR derived displacement values, a series of coherence values were used. High coherence values are equal to high data quality. The highest number of interferograms were from 2021, with a total of 8 interferograms. The coherence value was measured for each of the AOIs on each palsa, i.e. 5 coherence measurements for each interferogram, leading to 40 coherence measurements for per palsa. The number of interferograms from 2020 were 6 interferograms and resulting in 30 coherence measurements per palsa. The number of interferograms from 2019 were a total of 5 interferograms, giving 25 coherence measurements per palsa. Note that the measured coherence is based on pixel values over the different AOIs and not coherence over the whole interferogram. The coherence for each of the palsa types can be seen in the results section (section 4.3.).

4. Results

4.1. DInSAR results between 2019 to 2021

4.1.1. Reference data for the DInSAR results

Unfortunately no reference data to assess the accuracy of the DInSAR displacement was available for the project. During the field trip elevation measurements for one point in time were taken, as it was anticipated that this would suffice. Displacement measurements were not taken, as that would have required RTK-GPS measurements at two time points, which was not planned for. Therefore the following results (sections 4.1.2. to 4.1.4.) are strictly estimations.

4.1.2. DInSAR results for 2019

During the period 23rd of July to the 22nd of August, 2019, the majority of the investigated areas on the dome palsa experienced a slight uplift, with the maximum displacement of 0.51 cm (Figure 11, 5th AOI). Similarly the majority of the investigated areas on the ridge palsa experienced slight uplift, with the highest displacement reaching 0.49 cm (Figure 12, 3rd AOI). The mean air temperature during this period was around 11°C, while the highest recorded temperature was around 25°C (the 27th of July), and the lowest around -4°C (the 5th of August). High amounts of precipitation occurred during this period, indicating a wet period (Table 4).

From the 22nd of August to 3rd of September all of the investigated areas on the dome palsa subsided, with the maximum displacement of -2.27 cm (Figure 11, 5th AOI). Similar trends can be observed at the ridge palsa where all of the investigated areas also experienced subsidence, with the maximum displacement of -1.57 cm (Figure 12, 3rd AOI). During this period the mean air temperature was around 12°C, with the highest recorded air temperature around 23°C (the 28th of August) and the lowest around 4°C (26th of August). Relatively high amounts of precipitation occurred during this period, indicating a relatively wet period (Table 4).

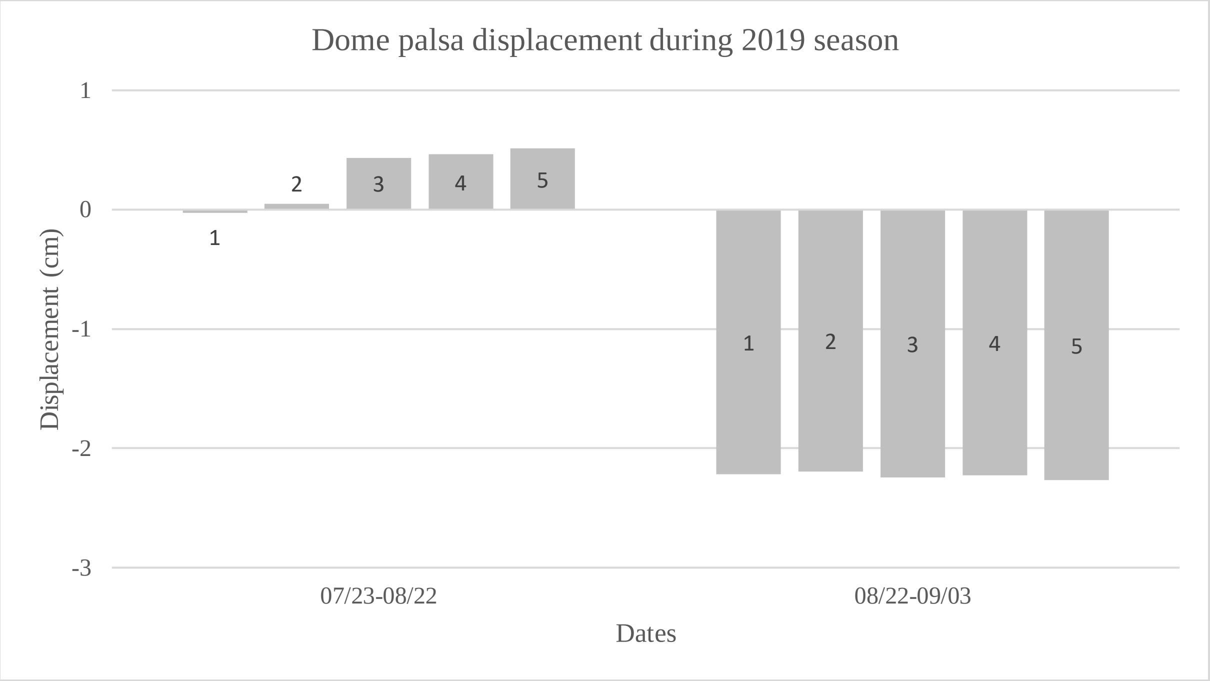

Figure 11: Mean displacement values for the dome palsa from July to September during the 2019 season. The numbering represents the different AOIs on the dome palsa (Figure 5).

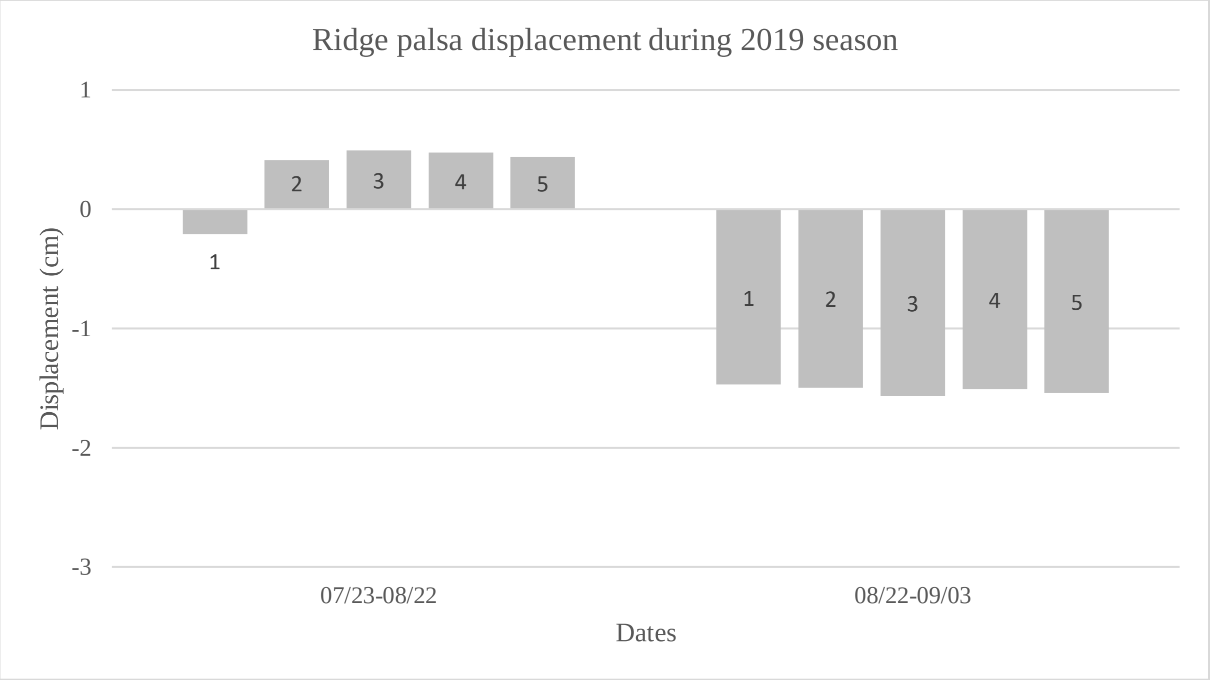

Figure 12: Mean displacement values for the ridge palsa from July to September during the 2019 season. The numbering represents the different AOIs on the ridge palsa (Figure 6).

Table 4: Meteorological data for the 2019 season displaying the mean, maximum, minimum air temperature and total amount of precipitation. The dates in parentheses are the dates when the maximum and minimum air temperatures were recorded respectively. The temperature data have been compensated for elevation differences between the weather station at Naimakka and the location of the study area, while the precipitation data is directly derived from the Naimakka weather station.

Date	Mean air temperature (°C)	Maximum air temperature (°C)	Minimum air temperature (°C)	Total amount of precipitation (mm)
07/23-08/22	10.83	25.25 (07/27)	-3.65 (08/05)	78.2
08/22-09/03	11.78	22.85 (08/28)	4.35 (08/26)	34.7

4.1.3. DInSAR results for 2020

From the 5th of July to the 4th of August, 2020, all of the investigated areas on the dome palsa experienced slight uplift, with the maximum displacement reaching 1.70 cm (Figure 13, 3rd AOI). The ridge palsa displacement however, displayed a slight net subsidence in the investigated areas, with the maximum displacement reaching -0.19 cm (Figure 14, 1st AOI). During this period the mean air temperature was around 12°C, the highest recorded temperature around 21°C (the 17th of July) and the lowest around 2°C (the 3rd of August). Large amounts of precipitation occurred during this period, indicating a wet period (Table 5).

During the period from the 4th of August to the 3rd of September all of the investigated areas on the dome palsa subsided, with the maximum displacement reaching -1.03 cm (Figure 13, 5th AOI). A slight subsidence also occurred in the investigated areas of the ridge palsa, with the maximum displacement reaching -0.76 cm (Figure 14, 4th AOI). The mean air temperature during this period was around 10°C, and the highest recorded temperature around 22°C (the 8th of August) and lowest temperature around -3°C (the 31st of August). Relatively large amounts of precipitation occurred during this period, indicating a relatively wet period (Table 5).

From the 3rd to the 15th of September all the investigated areas on the dome palsa experienced a slight uplift, with the maximum displacement reaching 0.77 cm (Figure 13, 3rd AOI). The investigated areas on the ridge palsa however experienced a slight subsidence, with the maximum displacement reaching -0.12 cm (Figure 14, 4th AOI). During this period the mean air temperature was around 7°C, the highest air temperature recorded was around 14°C (the 3rd of September) and the lowest around -3°C (the 13th of September). The amount of precipitation this period was relatively low in comparison to previous periods this season, but high enough to indicate a fairly wet period (Table 5).

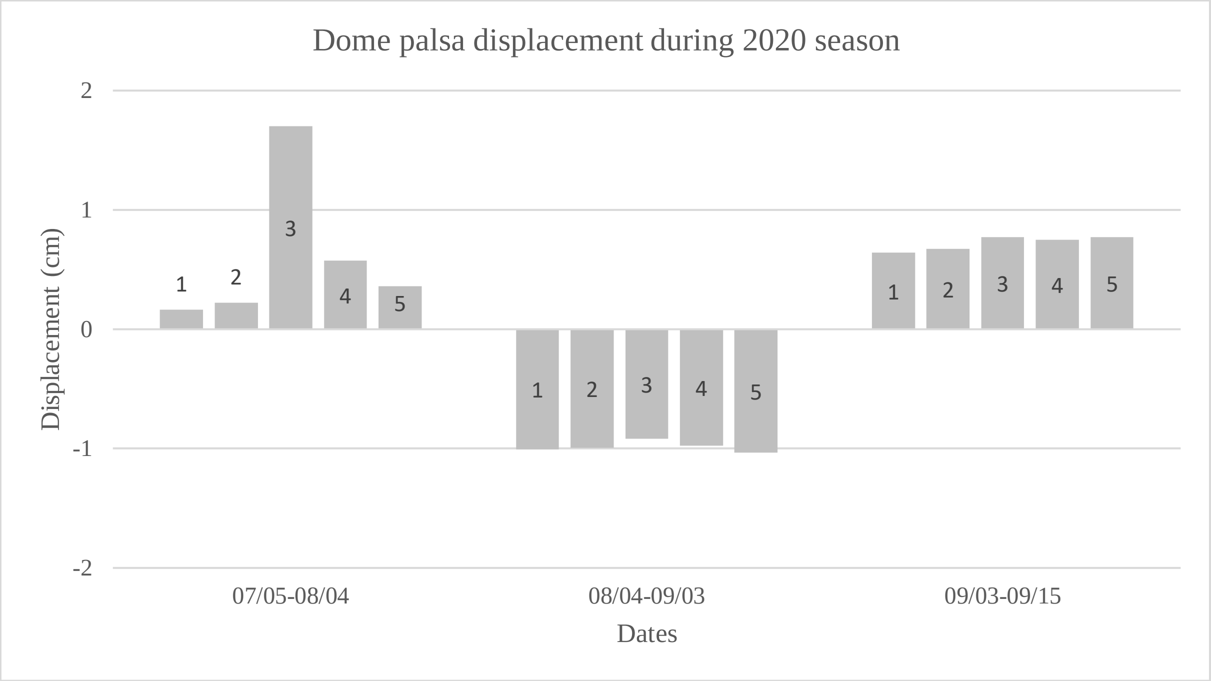

Figure 13: Mean displacement values for the dome palsa from July to September during the 2020 season. The numbering represents the different AOIs on the dome palsa (Figure 5).

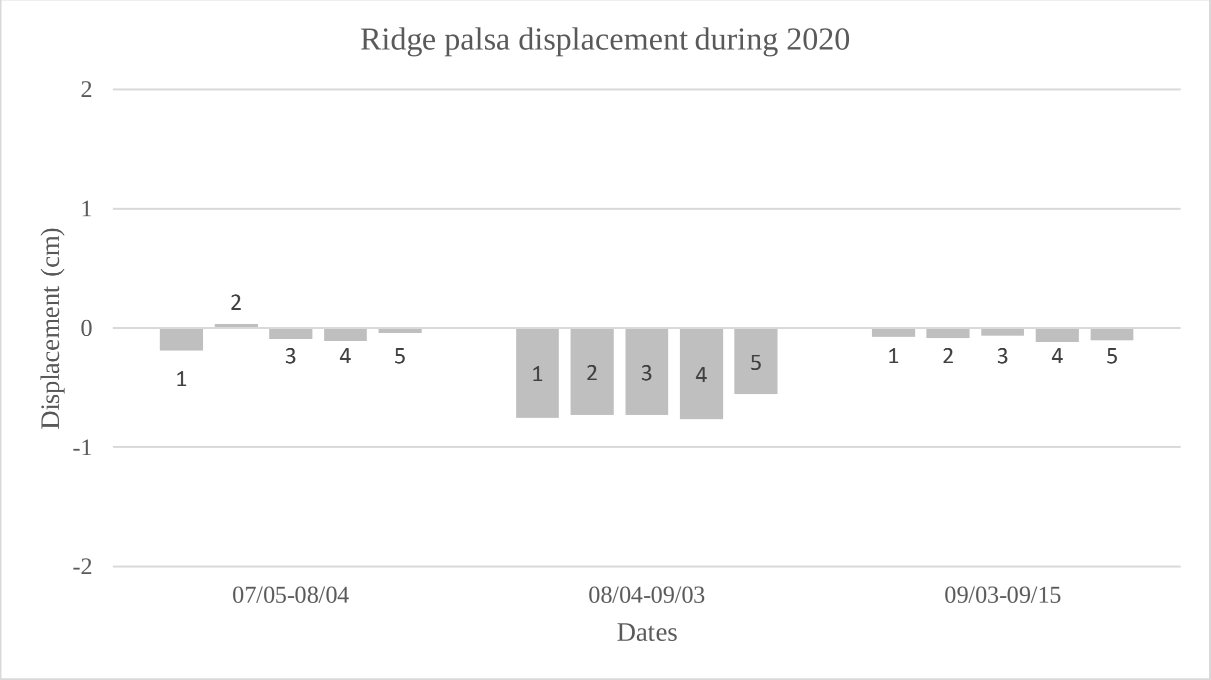

Figure 14: Mean displacement values for the ridge palsa mire from July to September during the 2020 season. The numbering represents the different AOIs on the ridge palsa mire (Figure 6).

Table 5: Meteorological data for the 2020 season displaying the mean, maximum, minimum air temperature and total amount of precipitation. The dates in parentheses are the dates when the maximum and minimum air temperatures were recorded respectively. The temperature data have been compensated for elevation differences between the weather station at Naimakka and the location of the study area, while the precipitation data is directly derived from the Naimakka weather station.

Date	Mean air temperature (°C)	Maximum air temperature (°C)	Minimum air temperature (°C)	Total amount of precipitation (mm)
07/05-08/04	11.61	21.15 (07/17)	1.55 (08/03)	125.1
08/04-09/03	9.46	22.15 (08/08)	-3.35 (08/31)	76.7
09/03-09/15	6.7	14.15 (09/03)	-2.65 (09/13)	36.9

4.1.4. DInSAR results for 2021

During the period from the 6th to 24th of July, 2021, all investigated sites on the dome palsa subsided, with the maximum displacement reaching -1.34 cm (Figure 15, 1st AOI). Similarly all the investigated sites on the ridge palsa also subsided during this period, with the maximum displacement reaching -1.22 cm (Figure 16, 2nd AOI). Between the 6th to 24th of July the mean air temperature was around 12°C, and the highest air temperature recorded during this period was around 25°C (the 7th of July), while the lowest was around 3°C (the 20th of July). Low amounts of precipitation occurred during this period, indicating a relatively dry period (Table 6).

During the period from the 24th of July to the 5th of August all investigated sites on the dome palsa subsided, with the maximum displacment reaching -1.15 cm (Figure 15, 2nd AOI). Similar subsidence trends could be observed at the ridge palsa, with the maximum displacement reaching -0.95 cm (Figure 16, 5th AOI). During this period the mean air temperature was around 11°C, and the highest air temperature recorded was around 26°C (the 28th of July) and the lowest around -2°C (the 3rd of August). Very low amounts of percipitation occurred during this period, indicating a very dry period (Table 6).

During the period from the 5th to 23rd of August most of the investigated areas on the dome palsa displayed no displacement, while some areas display a slight uplift with maximum displacement reaching 0.32 cm (Figure 15, 2nd AOI). All the investigated areas on the ridge palsa displayed slight uplift, with the highest displacement reaching 0.59 cm (Figure 16, 1st AOI). During this period the mean air temperature was around 10°C, while the highest air temperature recorded was around 21°C (the 7th of August) and the lowest around -3°C (the 18th of August). Fairly high amounts of precipitation occurred during this period, which indicates a fairly wet period (Table 6).

During the period from the 23rd of August to 4th of September all of the investigated areas on the dome palsa expericened uplift, with the maximum displacement reaching 3.30 cm

(Figure 15, 5th AOI). Similar uplifting trends can be observed on the ridge palsa, with the maximum displacement reaching 2.43 cm (Figure 16, 1st AOI). During this period the mean air temperature was around 7°C, and the highest air temperature recorded was around 16°C (the 27th of August) and the lowest -2°C (the 29th of August). Very small amounts of precipitation occurred during this period, indicating a very dry period (Table 6).

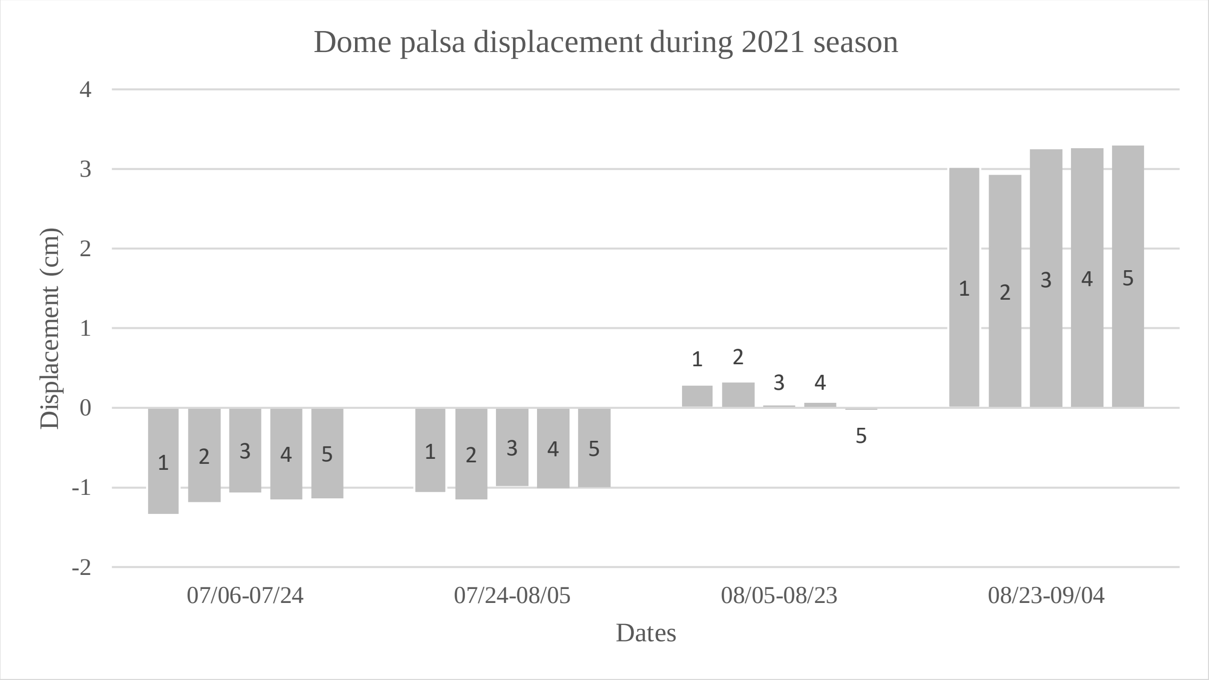

Figure 15: Mean displacement values for the dome palsa from July to September during the 2021 season. The numbering represents the different AOIs on the dome palsa (Figure 5).

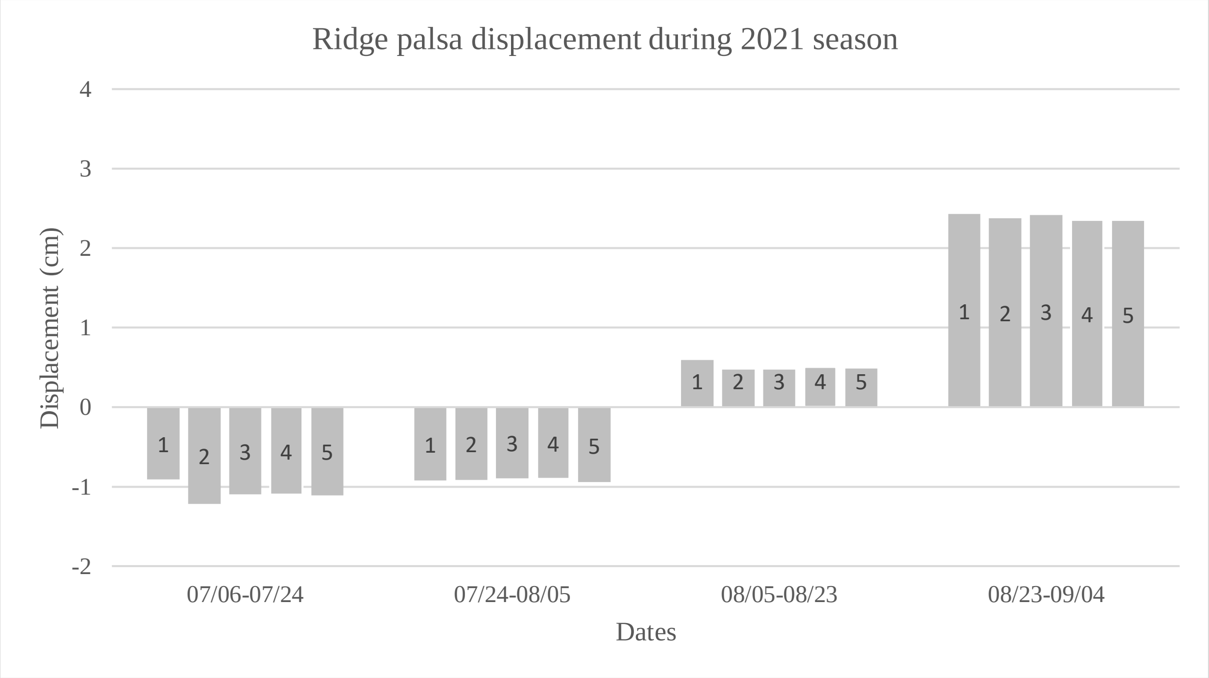

Figure 16: Mean displacement values for the ridge palsa from July to September during the 2021 season. The numbering represents the different AOIs on the ridge palsa (Figure 6).

Table 6: Meteorological data for the 2021 season displaying the mean, maximum, minimum air temperature and total amount of precipitation. The dates in parentheses are the dates when the maximum and minimum air temperatures were recorded respectively. The temperature data have been compensated for elevation differences between the weather station at Naimakka and the location of the study area, while the precipitation data is directly derived from the Naimakka weather station.

Date	**Mean air temperature (℃)**	**Maximum air temperature (℃)**	**Minimum air temperature (℃)**	**Total amount of precipitation (mm)**
07/06-07/24	12.45	24.65 (07/07)	2.95 (07/20)	13.5
07/24-08/05	10.96	25.65 (07/28)	-1.55 (08/03)	6.6
08/05-08/23	9.92	20.55 (08/07)	-2.95 (08/18)	48.2
08/23-09/04	6.59	16.45 (08/27)	-2.05 (08/29)	3.1

4.2. Relationships between displacement and meteorological conditions

4.2.1. Relationships between the dome palsa and meteorological conditions

There was an intermediate relationship between the mean air temperature and the displacement values (R^2 = 0.5238), which showed a negative trend, where higher mean temperatures were associated with higher values of subsidence of the dome palsa (Figure 17). The relationship between the maximum air temperature and displacement values was relatively intermediate (R^2 = 0.4238), where increases in maximum temperature leads to higher values of subsidence of the dome palsa (Figure 18). The relationship between the minimum air temperature and the displacement values was weak (R^2 = 0.2247), where higher minimum temperature lead to increased subsidence of the dome palsa (Figure 19). However this relationship was the weakest among the temperature variables. The relationship between the total amount of precipitation and the displacement values was non-existent (R^2 = 0.0009).

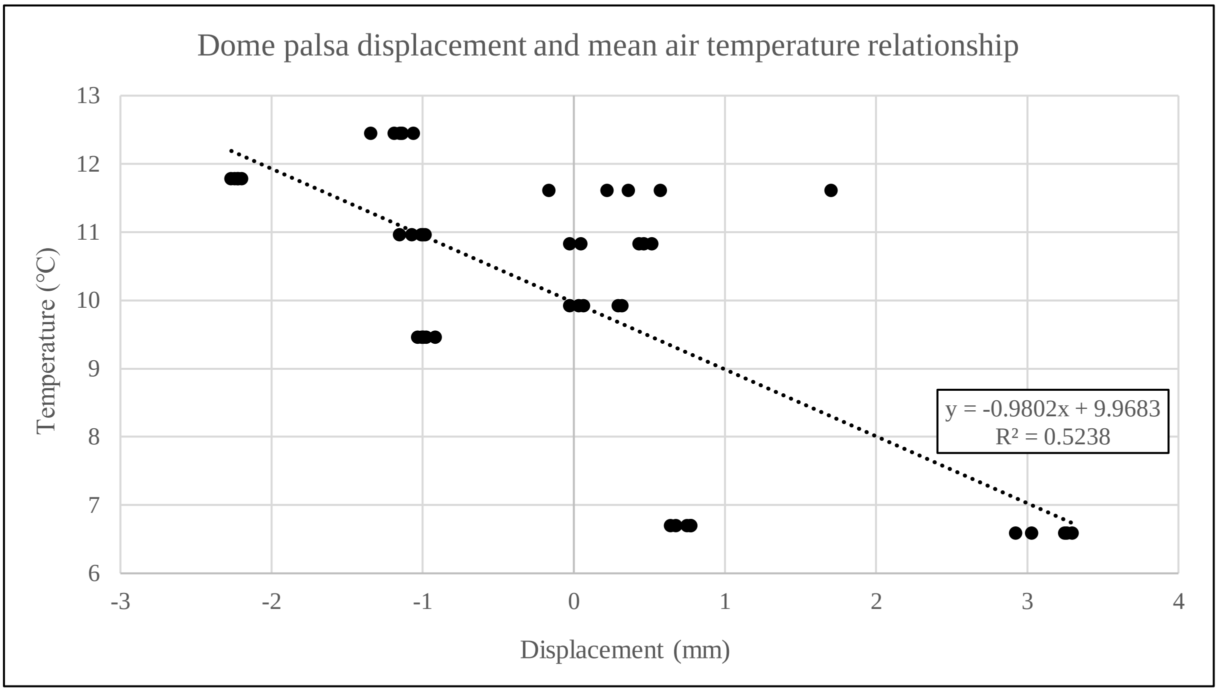

Figure 17: Relationship between the dome palsa displacement values and the mean air temperature from all respective season.

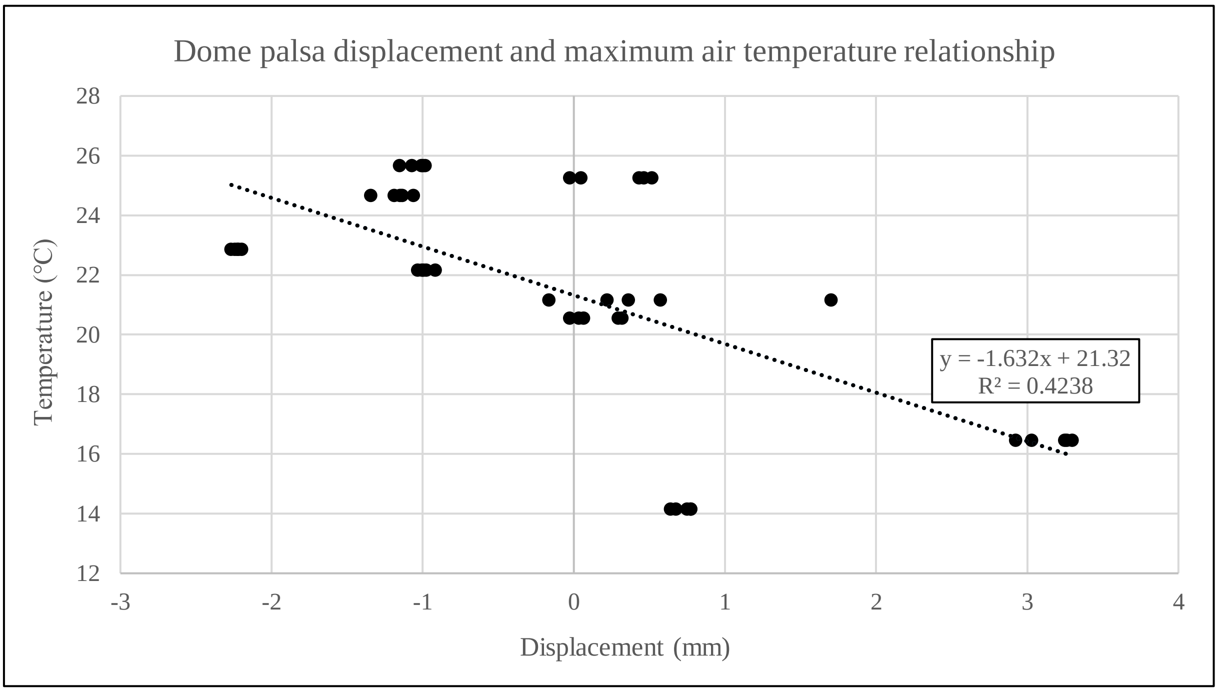

Figure 18: Relationship between the dome palsa displacement values and the maximum air temperature from all respective seasons.

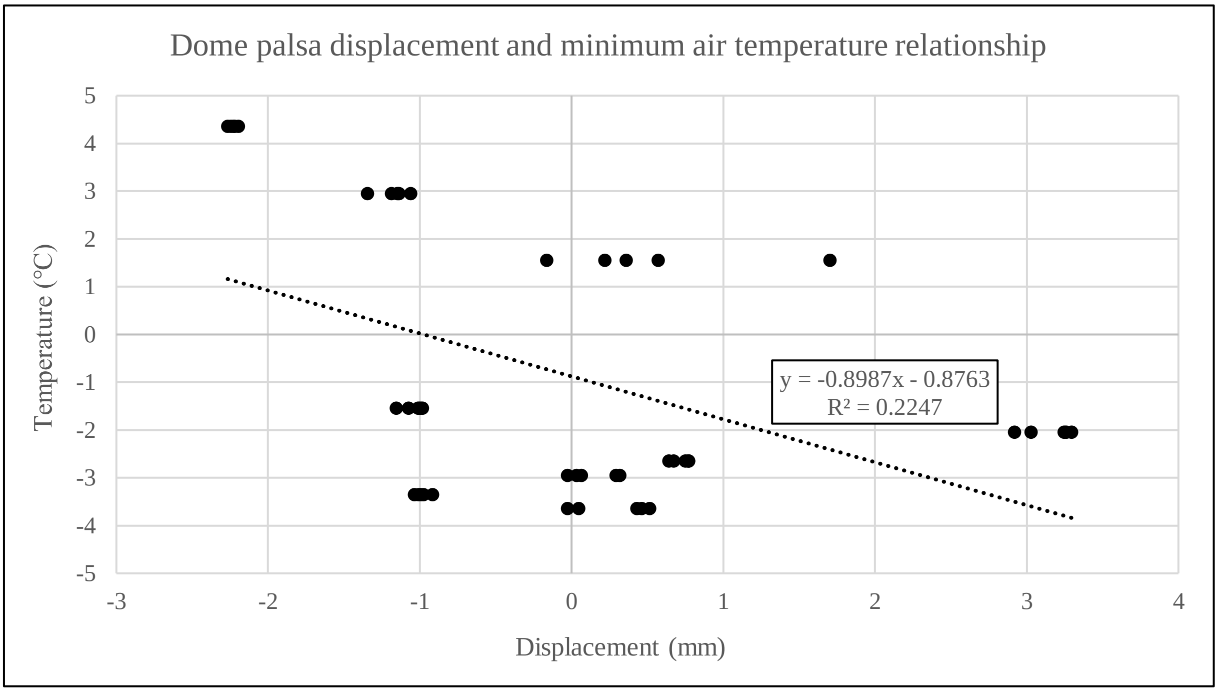

Figure 19: Relationship between the dome palsa displacement values and the minimum air temperature from all respective seasons.

4.2.2. Relationships between the ridge palsa and meteorological conditions

The relationship between the mean air temperature and the displacement values was intermediate (R^2 = 0.4697), where higher air temperatures led to an increased subsidence of the ridge palsa (Figure 20). The relationship between the maximum air temperature and displacement values was weak (R^2 = 0.3119), where higher maximum temperatures led to increased subsidence of the ridge palsa (Figure 21). Similarly the relationship between the minimum air temperature and the displacement values was also weak (R^2 = 0.2712), where higher minimum temperatures led to increased subsidence of the ridge palsa (Figure 22). There was no relationship between the total amount of precipitation and the displacement values (R^2 = 0.0057).

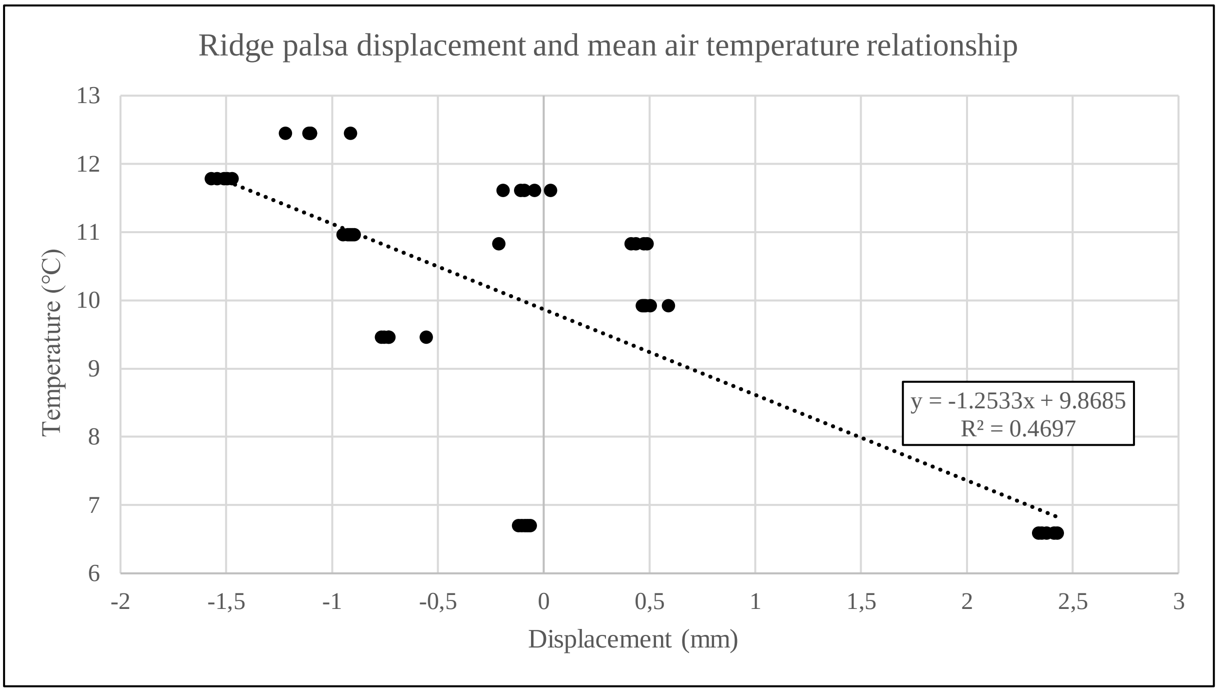

Figure 20: Relationship between the dome palsa displacement values and the mean air temperature from all respective seasons.

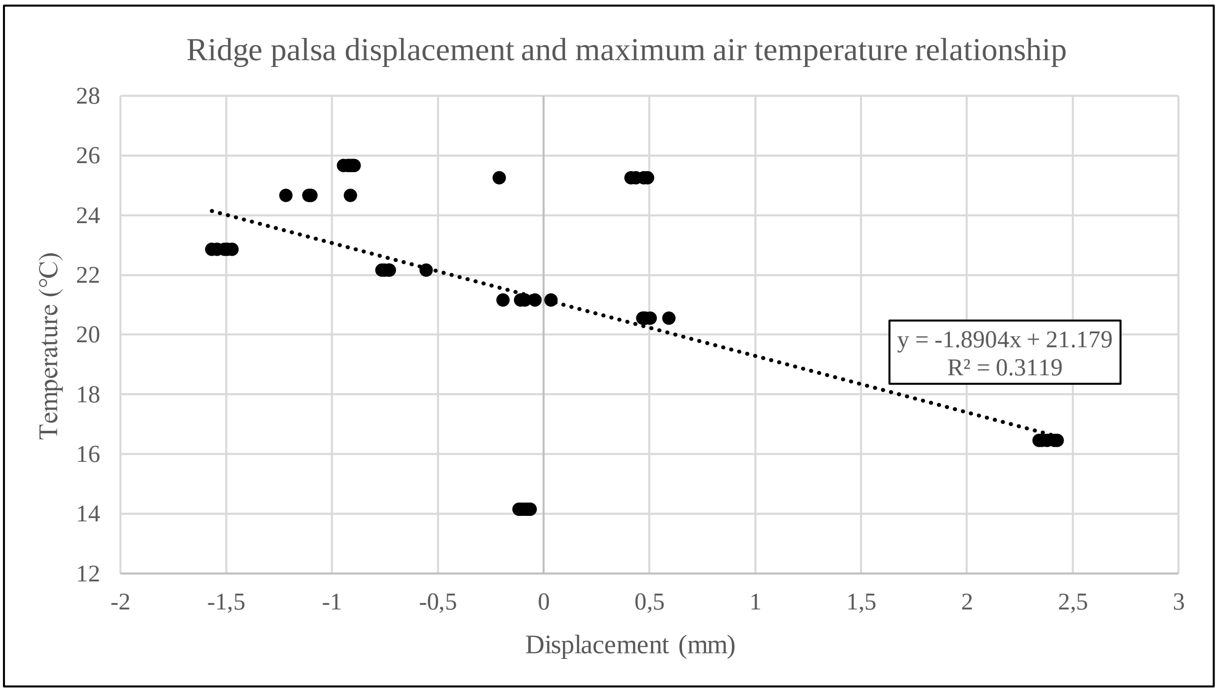

Figure 21: Relationship between the dome palsa displacement values and the maximum air temperature from all respective seasons.

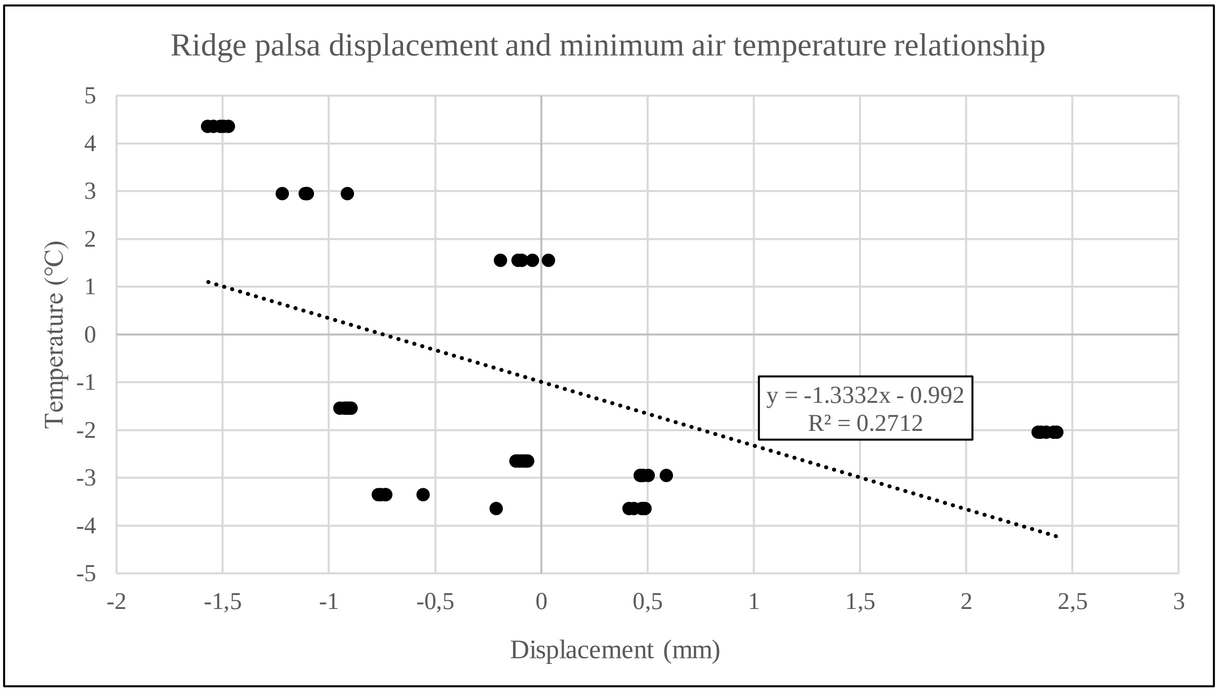

Figure 22: Relationship between the dome palsa displacement values and the minimum air temperature from all respective seasons.

4.3. Coherence estimation

4.3.1. Coherence over the dome palsa

During 2019 the measured coherence was considerably high in all of the interferograms, except maybe the interferogram from the 29th of June to 22nd of August, which had relatively low coherence (Table 7).

During 2020 the measured coherence was also relatively high, however sometimes the measured coherence was very low, especially for the interferogram from 11th of June to 4th of August (Table 7).

During 2021 the measured coherence was exceptionally high, with only one of the coherence measurements below 50% (Table 7).

Table 7: A summary of the pixel coherence in percentage for each of the AOIs within each interferogram used in the project over the dome palsa mire, between 2019 to 2021 season. Green markings indicate coherence values near or above 50%, orange markings indicate coherence near or within 33 to 45%, and lastly red markings indicate coherence lower than or near 33%.

Interferogram	1st AOI	2nd AOI	3rd AOI	4th AOI	5th AOI
19/07/23-29	57.3	60.4	50.4	53.6	30.8
19/07/29-08/22	54.6	47.4	14.6	11.1	8.5
19/08/22-28	65.3	68.7	60.7	61.6	67.6
19/08/28-09/03	49.7	41.1	75.1	69.4	77.3
20/07/05-11	60.5	54.8	37.7	39.2	28.1
20/07/11-08/04	25.0	21.3	8.7	20.6	28.6

20/08/04-10	59.1	62.5	50.6	39.8	49.0
20/08/10-09/03	58.6	55.3	26.1	27.2	42.3
20/09/03-09	22.1	38.9	49.4	69.6	58.2
20/09/09-15	63.2	53.3	82.1	78.4	73.9
21/07/06-18	49.4	49.4	39.1	50.5	54.6
21/07/18-24	57.7	58.0	76.3	71.6	74.2
21/07/24-30	57.9	66.8	58.6	64.4	69.2
21/07/30-08/05	76.6	78.5	72.0	75.4	72.4
21/08/05-17	62.3	68.7	71.8	76.3	58.5
21/08/17-23	51.0	54.5	54.8	68.8	58.5
21/08/23-29	46.0	53.2	53.5	59.6	66.5
21/08/29-09/04	74.4	74.5	72.4	75.6	76.7

4.3.2. Coherence over the ridge palsa

During 2019 the measured coherence was relatively intermediate, with half of the measured coherence exceeding 50% (Table 8, green values), and half of the measurement below 50% (Table 8, orange and red values).

During 2020 the measured coherence was lower, with the majority of the measurements indicating coherence below 50% (Table 8, orange and red values).

During 2021 the measured coherence was much higher when compared to previous years, however some of the interferograms covering the latter part of the season can have relatively low coherence (Table 8).

Table 8: A summary of the pixel coherence in percentage for each of the AOIs within each interferogram used in the project over the ridge palsa mire, between 2019 to 2021 season. Green markings indicate coherence values near or above 50%, orange markings indicate coherence near or within 33 to 45%, and lastly red markings indicate coherence lower than or near 33%.

Interferogram	**1st AOI**	**2nd AOI**	**3rd AOI**	**4th AOI**	**5th AOI**
19/07/23-29	42.3	22.2	43.8	47.8	60.9
19/07/29-08/22	23.2	28.6	35.2	45.0	49.2
19/08/22-28	61.9	67.8	73.7	77.2	76.6
19/08/28-09/03	49.3	31.4	33.0	43.3	44.1
20/07/05-11	43.8	38.9	35.4	54.2	16.0
20/07/11-08/04	47.0	38.9	33.0	32.5	27.2
20/08/04-10	45.9	37.5	51.3	43.2	40.0
20/08/10-09/03	22.8	17.6	33.9	46.2	31.9
20/09/03-09	46.7	49.5	44.5	33.4	0.0

20/09/09-15	40.9	39.5	44.5	61.2	52.6
21/07/06-18	33.7	52.7	51.8	63.5	48.5
21/07/18-24	53.6	41.8	45.6	59.8	51.7
21/07/24-30	40.9	43.4	44.5	62.7	48.7
21/07/30-08/05	47.1	57.8	69.0	74.0	71.4
21/08/05-17	44.4	51.1	61.0	67.9	74.7
21/08/17-23	36.8	31.9	21.4	25.9	30.7
21/08/23-29	29.2	25.4	23.7	40.9	49.7
21/08/29-09/04	20,8	35.7	42.5	53.9	63.6

4.4. DInSAR DEM result

No high quality InSAR derived DEM could be created, due to either potential SAR image pairs exhibiting high temporal decorrelation or being affected by seasonal factors. Therefore the elevation reference points taken during the field trip could not be used unfortunately. A thorough discussion of this is given in Section 5.1.5.

5. Discussion

5.1. Results discussion

5.1.1. DInSAR displacement 2019

The period of the 23rd of July to 22nd of August, 2019, was a relatively warm period (highest recorded temperature was around 25°C), which in theory should lead to net subsidence of the palsa mires. However, there was an uplift of 0.51 cm in the dome palsa and 0.49 cm in the ridge palsa. The minimum air temperature during this time (around -4°C) indicated the possibility of the air temperature (and ground temperature) reaching subzero temperatures during this period, probably during nighttime, which should enable some of the permafrost to refreeze. A potential explanation for the net uplifting trends of the palsa this month are these potential nighttime refreezing events. However keep in mind that these uplifting trends are rather small and some of the investigated areas on both palsas actually experienced subsidence instead
(e.g. the 1st AOI in Figure 11 and 12 respectively).

Both the mean and maximum air temperature of 22nd of August to the 3rd of September was still relatively high when compared to the previous period (around 12°C and 23°C, respectively), which by itself could explain the net palsa mire subsidence observed during this period (dome palsa: -2.27 cm, and ridge palsa: -1.57 cm). However a potential cause of subsidence during this period may be the relatively high minimum air temperature of 4°C. The high minimum air temperature this period limits the number of occasions when the ground temperature could exceed subzero temperatures and begin refreezing when compared to the much lower air temperatures of the previous period.

5.1.2. DInSAR displacement 2020

There were differing results for the dome and ridge palsa during the 5th of July to the 8th of August, 2020, which had 1.70 cm uplift, and -0.19 cm subsidence, respectively. For this case it is more difficult to hypothesize the cause of this difference. There was a heavy amount of rainfall that occurred during this period (around 125 mm), which leads to more pore water in the palsa becoming available if refreezing would occur. Since the minimum air temperature during this period was around 2°C, this indicates that the ground temperature could probably reach below 0°C, and thus create potential refreezing events. The combination of these factors could lead to a small uplift of the palsa. However, there were potentially relatively high daily air temperatures during this season, as indicated by the highest recorded air temperature this period being around 21°C. In a warmer climate the number of thawing events may become greater for the permafrost inside the palsa than the number of refreezing events, and would therefore lead to a net thawing of the permafrost. The difference in displacements between the palsas could also depend on local factors, the dome palsa is located in a relatively open landscape next to a large lake (Vittankijärvi), while the ridge palsa is located with a large hill to the east. During fieldwork on these palsas in September 2021, I experienced that it was fairly windy on the dome palsa when compared to the calmer breezes at the ridge palsa, small differences like these may possibly lead to differences in displacement for the respective palsa.

The displacement trends from the 8th of August to the 3rd of September display a net subsiding rate, which probably depends on the still relatively high maximum air temperature of 22°C. Warmer temperatures leads to a net increase in the amount of thawing events inside the palsas, which causes subsidence in return.

During the 3rd to 15th of September there was a rather large change in both mean air temperature and maximum air temperature in comparison to the 8th of August to the 3rd of September (from around 10°C down to 7°C, and around 22°C down to 14°C, respectively), yet only small amounts of displacements occurred for respective palsa. This is similar to the trends seen during the 8th of August to the 3rd of September, and is again difficult to hypothesize about the cause, but may be due to local differences as explained before.

5.1.3. DInSAR displacement 2021

The subsiding trends in the palsa displacements during the 6th to 24th of July, 2021, were likely related to the high air temperatures (both maximum (25°C) and minimum (3°C)).

During the 24th of July to the 5th of August the meteorological conditions were very similar, and show a similar subsiding trend, although slightly lower. This might be explained by the lower minimum air temperature, which was below 0°C when compared to the previous period. The lower minimum air temperature may created potential refreezing, which acted as a brake in the subsiding trend during this period.

There was an uplifting trend in the palsas during the 5th to 23rd of August. During this time there was a relatively large decrease in the maximum air temperature (from around 26°C down to 21°C), in combination with high amounts of precipitation (from 6.6 mm up to 48.2 mm) compared to the previous period. The combination of colder and wetter conditions could lead to more suitable weather conditions for permafrost refreezing if the ground temperatures drops below 0°C. The refreezing potential is further increased by the high amounts of precipitation during this period, since precipitation leads to more porewater inside the palsas.

The largest uplifting trends of this study were seen during the 23rd of August to 4th of September. It is notable that there was relatively large decrease in both the mean and maximum air temperature (from around 10°C down to 7°C, and around 21°C down to 16°C, respectively) when compared to the previous period. As explained before a colder climate is better suited for permafrost refreezing and in combination with the fairly large precipitation that occurred the previous period could potentially lead to large permafrost refreezing events.

5.1.4. Relationship between displacement and meteorological conditions

Since none of the relationships between the various meteorological conditions and the displacement values were strong, it is difficult to establish if there exists any relationship between them. Therefore most of the DInSAR displacement discussion is based on logical theoretical reasoning (sections 5.1.1. to 5.1.3.), and not evidence based. However all of the temperature variables indicated a negative trend in relation to the displacement measurements, with increasing temperatures leading to palsa subsidence. Meaning that most of the theoretical reasoning in the DInSAR displacement discussion in theory could be true. On the other hand the relationship between precipitation and displacement values was non-existent, meaning that most of the theoretical reasoning behind porewater being available during permafrost refreezing events is questionable. Since this would indicate that there should exist some sort of relationship between palsa uplift (permafrost refreeze) and precipitation (porewater recharge).

5.1.5. DInSAR DEM

The SAR image pair needed to create a DInSAR derived DEM is recommended to have a perpendicular baseline from 150 meters up to 300 meters. Such image pairs exist over the study area, however these image pairs exhibit either high temporal decorrelation or are influenced by seasonal factors.

For SAR image pairs that can be used for DEM creation with a high enough perpendicular baseline, means that one image is acquired during wintertime, while the other one is acquired during summertime. This results both in high temporal decorrelation, and the resulting DInSAR derived DEM will also be affected by the snow cover present in the wintertime image; both of these factors lead to bad DEM/data quality. To achieve high coherence (and therefore high data quality), the image pair needs to have a low temporal baseline (i.e. the number of days elapsed between the different SAR images), and the lower the better. Since the potential image pair includes one image taken during summertime and the other one during wintertime, the temporal baseline would probably be > 100 days or more, and thus would create a DInSAR derived DEM of very low quality. The snow cover present in the wintertime image would further lead to a loss of coherence, since snow cover lowers the amount of backscattered radiation during image acquisition, as explained in the introduction (see section 1.2.1.). This problem is particular to the Sentinel-1 satellite, and a better satellite for the general purpose of DEM creation is the TanDEM-X satellite (Rizzoli et al., 2017).

5.2. Data quality

As summarized in the coherence estimation (see section 4.3.) the coherence value and therefore the data quality was increased with newer data, especially over the dome palsa region (see section 4.3.1.). This can also be observed in the number of interferograms that were used for each of the years, with the highest number of interferograms for 2021 (8 interferograms), for 2020 (6 interferograms), and the lowest number for 2019 (4 interferograms). However it is difficult to evaluate if the coherence values are high enough to accommodate good data quality, since the ridge palsa region exhibits much lower coherence overall (see section 4.3.2.). Therefore the displacement results may not be fully realistic, especially over the ridge palsa, and should be noted when trying to interpret the displacement measurements.

5.3. Result comparison with previous research

Similar to my situation, many previous permafrost studies also had no reference data to evaluate their results with. I have therefore focused on ways previous researchers suggests using InSAR data instead.

As suggested by Short et al. (2014) DInSAR derived seasonal ground displacement information is very useful for *identifying* problem areas, their extent and connections and for deducing possible causes in permafrost terrain. In their study they used RADARSAT-2 data to measure ground displacement at the Idaluit Airport at Baffin Island in Canada. Their results indicated that the DInSAR measurements worked well over areas which was well drained, but tended to underestimate the true displacement of the ground in areas that were saturated. Therefore their research suggest that DInSAR might work poorly for palsa mires, since they are relatively saturated. Similarly Rudy et al. (2018) suggested that DInSAR measurements in combination with both temperature and soil moisture data is useful for measuring seasonal ice aggradation and degradation, thus helping to *target* more detailed geophysical investigations in permafrost environments. In their study they also used RADARSAT-2 data to measure seasonal and multi-year surface displacements in the Canadian High Arctic. They also point out that their DInSAR measurements were not able to provide absolute values associated with aggradation and degradation of ice. Similar to Short et al. (2014), Rudy et al. (2018) also suggest the possibility that their DInSAR measurements underestimated the actual displacement throughout the summer season as the radar signal may be returned by the water table surrounding the permafrost.

Mohammadimanesh et al. (2019) when applying the InSAR SBAS method on RADARSAT-2 data found a correlation between the spatial extent of their displacement map and the surficial geology map in discontinuous permafrost terrain in Mayo, Yukon Territory, Canada. Specifically, unstable regions identified by InSAR were consisting of loose sediment such as moraine, glaciofluvial and glaciolacustrine sediments. This indicated that the SBAS method could indeed be used to map different sedimentology classes. They also suggested that the SBAS method works as a *baseline guide* for establishing future adaptation and mitigation plans and may also be used for scientific research in other cold regions with similar climatic characteristic. Wang et al. (2020) concluded that during the summer season, the SBAS method when using Sentinel-1 data yielded good displacement results in a sub-Arctic low shrub tundra environment above the tree line at their study site located in Northern Quebec, Canada. However, the accuracy was unpromising over developed shrub-tundra and, especially over forest-tundra environments, since the Sentinel-1 C-band did not penetrate the dense shrub canopy cover. This could explain the relatively low coherence over the investigated area, since both palsas in this project are located within shrub-tundra like vegetation, within the tree line. The palsas are also closely located to a large deciduous forest area and could be seen as similar to that of a forested-tundra (Figure 7, large hill).

Alshammari et al. (2020) suggest that ISBAS derived displacement results from Sentinel-1 data even thought they could not assess the accuracy of their data, can be considered sufficient for producing a meaningful signal that relates to peatland conditions and processes. They further suggest that their results could be used to support a satellite-based monitoring system on C-band SAR images that could be used for monitoring peatland condition. Their research uses so called Big InSAR data, which was comprised of 47 SAR images used to create more than 1000 interferograms over 22 peatland site in the Flow Country of northern Scotland. Therefore there results exhibited high redundancy and good precision, with displacement measuring accuracy below 2 mm. As their research suggests there is a possibility for larger investigations by using InSAR-data, however its feasibility for a single person is low, since processing these amounts of data takes a considerable amount of time. Even computer with high processing potential, by my own experience. Similar to the other studies mentioned before, de la Barreda-Bautista et al. (2022) suggests the ISBAS method should be used as a tool for subsidence detection resulting from recent permafrost degradation events and landscape-scale understanding of the vulnerabilities linked to subsidence. Similar to other studies their ISBAS displacement values were underestimated when compared to their reference displacement values. Similar to Alshammari et al. (2020), de la Barreda-Bautista et al. (2022) also used big InSAR data comprised of 125 SAR images from Sentinel-1 used to produce almost 1900 interferograms over three peatlands located to the south of Lake Torneträsk, northern Sweden. Their reference data consisted of RGB images taken from a drone, which was processed into DEMs and compared to the ISBAS derived displacement values. Their study area was located close to my study area. Their research suggests that even with Big InSAR data sets, the displacement values will still underestimate the actual displacement, due to low spatial resolution or temporal decorrelation of the Sentinel 1 data.

Since most of the previous research that have used InSAR methods, usually underestimated the real displacement that have occurred. I would, like most of the previous research, suggest that InSAR data should be used as a tool to *identify* potential areas that are undergoing either subsidence or uplift. For detailed displacement analysis I would suggest using data that is of higher spatial resolution than that of Sentinel-1, e.g. DEM data derived from drone data, similar to what de la Barreda-Bautista et al. (2022) have used in their report.

5.4. Improving the results

The major limiting factor of the project was the limited amount of Sentinel-1 data available over the study area. The amount of good available SAR imagery since 2014 until 2021 (2014 was the year which the first Sentinel-1 satellite became spaceborne) is more or less used in this project. To obtain more SAR data one would need to use other older satellite data from e.g. ERS-2 or ENVISAT (in orbit from 1995-2011 and 2002-2012, respectively, Meyer, 2019)), however then new problems may arise since both these satellites have completely different repeat cycles when compared to the newer Sentinel-1 satellite (both ERS-2 and ENVISAT have repeat cycles of 35 days, while Sentinel has 6 days (Meyer, 2019)). This in turn affects the coherence of the images, since the temporal baseline would become much higher and thus lead to temporal decorrelation of the SAR images as explained before (see section 1.2.1.).

Another problem with using older satellite data is the lower resolution of the data, e.g. ERS-2 has a pixel resolution of ranging from 6 × 26 m to 30 × 26 m and the ENVISAT 28 × 28 m, which is much lower than for the Sentinel-1 IW 5 × 20 m (Meyer, 2019). This means that the processed DInSAR data from these lower pixel resolution, probably will create a lower resolution than the DInSAR data used in this project (10 × 10 m). Therefore trying to investigate smaller landforms such as palsa mires is considerably harder, since using the higher resolution of Sentinel-1 IW (and the processed data from it) for this purpose is already a challenge. This is also pointed out as a limiting factor by e.g. Wang et al. (2020).

Another major limiting factor of the data used in the project is the relatively high sensitivity to weather conditions for Sentinel-1 data. Good Sentinel-1 data is dependent on good weather conditions, with ideally sunny weather with no precipitation and low wind speeds. In reality these weather conditions are uncommon in the study area, since precipitation is quite abundant over the whole season. The major problem with Sentinel-1 data is its high sensitivity towards snow, since snow can drastically change the backscatter radiation capabilities of the satellite microwaves during image acquisition (see section 1.2.1.). This in return lowers the coherence of the InSAR interferograms. Usually snow starts to settle in the area during late September and most of the snow has melted away in late June. However some perennial snow may still be present in the area during the whole season, mostly on or close to mountain tops. So most of the potentially useful SAR images are limited to the period between late June and late September, around two and a half months. This means that the majority of the seasonal dynamics of the palsa mires cannot be analyzed with only InSAR data and the need for other complementary data is needed instead. Therefore most of the research using InSAR data, not only for permafrost or peatland investigations, almost always use other types of complementary data (e.g. aerial photographs, drone data or optical satellite data) to analyze seasonal periods where InSAR data are inappropriate. Not surprisingly during a large recent literature review summarized by Philipp et al. (2021) were they reviewed over 300 articles directly linked to permafrost related remote sensing analyses. Over 55% of the reviewed articles were still using optical satellite imagery, followed by SAR images (20%).

The quality of the data would probably also be improved (and therefore the displacement results), especially the coherence, with the use of the ISBAS method instead of the DInSAR method used in this study (see section 1.2.2.). It would be especially interesting to see the difference of the displacement values when comparing results from these two methods. However it is likely that the end result would become similar, due to the low amount of good data available over the study area that can be used in either methods. Also as suggested by Alshammari et al. (2020), they would not anticipate good results with the ISBAS method if the total number of SAR images over the investigated area were lower than 30. Therefore it is questionable if the ISBAS method would actually produce better displacement results in this project, since the total number of images used in this project was only 21.

It would also be interesting to have on site measurements, especially for investigating meteorological parameters and their documented effects on the permafrost within the palsa, e.g. wind speed for wind erosion, groundwater flow to investigate its effect on thaw patterns etc. (see section 1.2.5.). On site measurements would also eliminate the need for height compensating the climate data from Naimakka weather station, and could therefore lead to better results when trying to investigate the relationship between displacement values and the various meteorological conditions (section 4.2.).

6. Conclusion

Based on the research questions in the beginning of the report the following conclusions can be drawn:

- No consistent seasonal elevation dynamics could be seen for either of the investigated palsas. This was primarily because the displacement values differed too much between the palsas during the same investigated period. It was also difficult to draw any conclusions due to the lack of reference data in the project, resulting in no possibility to assess the accuracy of the data. Another limiting factor was the high sensitivity of SAR data to weather conditions, especially precipitation and snow, limiting the usability of SAR data to around two and a half months per year at best circumstances. Therefore it was not possible to investigate seasonal dynamics other than during the summer months.
- Relationships between the elevation dynamics for the individual palsas and the various meteorological conditions did not show large coefficient of determination (R^2). The

highest R^2 was 0.5238 between the mean air temperature and the dome palsa displacement. Similarly R^2 was 0.4697 between the mean air temperature and the ridge palsa. However there was a negative trend associated with temperature variables and the measured displacement of the palsas. In general, warmer temperatures were associated with subsidence for both the dome and ridge palsa.

- No high quality DInSAR derived Digital Elevation Model (DEM) could be created over the study area. This was mainly because the data properties needed within the SAR-data (i.e. high enough perpendicular baseline, with low enough temporal baseline) did not exists over the study area.

To summarize, DInSAR derived displacement data is useful for those who are applying an investigation involving ground deformation in a wider remotely located study area, but are uncertain where in the study area to conduct the investigation. Based on the displacement result from the DInSAR data, the potential investigated area can then be narrowed down to a smaller study area. But for more detailed investigation, other higher spatial resolution data, such as DEM data from drone RGB images, should be considered.

7. Acknowledgments

I would like to thank Heather Reese at University of Gothenburg for being my supervisor throughout the project. Mats Olvmo at University of Gothenburg for helping me with the fieldwork in Saarikoski as well as being my examiner. My course mate Malin for being my opponent during my thesis defense. My mom for her involvement and support during the project. My dad for helping me build and finance the desktop used to process the data for this project.

8. References

Alshammari, L., Boyd, D. S., Sowter, A., Marshall, C., Andersen, R., Gilbert, P., Marsh, S., & Large, D. J. (2020). Use of Surface Motion Characteristics Determined by InSAR to Assess Peatland Condition [Article]. *Journal of Geophysical Research: Biogeosciences*, *125*(1), Article e2018JG004953. https://doi.org/10.1029/2018JG004953

Backe, S. (2014). *Kartering av Sveriges palsmyrar*. Länsstyrelsen.

Bamler, R., & Hartl, P. (1998). Synthetic aperture radar interferometry. *Inverse problems*, *14*(4), R1.

Berardino, P., Fornaro, G., Lanari, R., & Sansosti, E. (2002). A new algorithm for surface deformation monitoring based on small baseline differential SAR interferograms. *IEEE Transactions on Geoscience and Remote Sensing*, *40*(11), 2375-2383.

Borge, A. F., Westermann, S., Solheim, I., & Etzelmüller, B. (2017). Strong degradation of palsas and peat plateaus in northern Norway during the last 60 years. *The Cryosphere*, *11*(1), 1-16.

Braun. (2021). Retrieval of digital elevation models from Sentinel-1 radar data – open applications, techniques, and limitations. *Open Geosciences*, *13*(1), 532-569. https://doi.org/doi:10.1515/geo-2020-0246

Braun, A., & Veci, L. (2021). TOPS Interferometry Tutorial. *Array Systems. Available online: http://step. esa. int/docs/tutorials/S1TBX% 20TOPSAR% 20Interferometry% 20with% 20Sentinel-1% 20Tutorial_v2. pdf (accessed March 2022)*.

Brown, J., Ferrians, O., Heginbottom, J., & Melnikov, E. (2002). Circum-Arctic map of permafrost and ground-ice conditions, version 2. *Boulder, Colorado USA, National Snow and Ice Data Center*.

Chen, C. W., & Zebker, H. A. (2000). Network approaches to two-dimensional phase unwrapping: intractability and two new algorithms. *JOSA A*, *17*(3), 401-414.

Chen, C. W., & Zebker, H. A. (2001). Two-dimensional phase unwrapping with use of statistical models for cost functions in nonlinear optimization. *JOSA A*, *18*(2), 338-351.

Chen, C. W., & Zebker, H. A. (2002). Phase unwrapping for large SAR interferograms: Statistical segmentation and generalized network models. *IEEE Transactions on Geoscience and Remote Sensing*, *40*(8), 1709-1719.

Cigna, F., & Sowter, A. (2017). The relationship between intermittent coherence and precision of ISBAS InSAR ground motion velocities: ERS-1/2 case studies in the UK. *Remote Sensing of Environment*, *202*, 177-198.

de la Barreda-Bautista, B., Boyd, D. S., Ledger, M., Siewert, M. B., Chandler, C., Bradley, A. V., Gee, D., Large, D. J., Olofsson, J., Sowter, A., & Sjögersten, S. (2022). Towards a Monitoring Approach for Understanding Permafrost Degradation and Linked Subsidence in Arctic Peatlands. *Remote Sensing*, *14*(3), 444. https://www.mdpi.com/2072-4292/14/3/444

ESA. (n.d.). *Misson Summary; Sentinel-1 Overview; SAR Instrument; Acquisition Modes;* . ESA. Retrieved 17/05 from https://sentinel.esa.int/web/sentinel/home

Ferretti, A., Monti-Guarnieri, A., Prati, C., & Rocca, F. (2007b). InSAR processing: part B: a practical approach. *Noordwijk, The Netherlands: ESA Publications*.

Ferretti, A., Monti-Guarnieri, A., Prati, C., Rocca, F., & Massonnet, D. (2007a). Part A Interferometric SAR image processing and interpretation. *InSAR Principles: Guidelines for SAR Interferometry Processing and Interpretation, ESA Publications (http://www. esa. int/esapub/tm/tm19/TM-19_ptA. pdf)*.

Fronzek, S. (2013). Climate change and the future distribution of palsa mires: ensemble modelling, probabilities and uncertainties.

Gabriel, A. K., Goldstein, R. M., & Zebker, H. A. (1989). Mapping small elevation changes over large areas: Differential radar interferometry. *Journal of Geophysical Research: Solid Earth*, *94*(B7), 9183-9191.

Goldstein, R. M., & Werner, C. L. (1998). Radar interferogram filtering for geophysical applications. *Geophysical research letters*, *25*(21), 4035-4038.

Hugelius, G., Strauss, J., Zubrzycki, S., Harden, J. W., Schuur, E., Ping, C.-L., Schirrmeister, L., Grosse, G., Michaelson, G. J., & Koven, C. D. (2014). Estimated stocks of circumpolar permafrost carbon with quantified uncertainty ranges and identified data gaps. *Biogeosciences*, *11*(23), 6573-6593.

Johansson, M., Åkerman, J., Keuper, F., Christensen, T. R., Lantuit, H., & Callaghan, T. V. (2011). Past and Present Permafrost Temperatures in the Abisko Area: Redrilling of Boreholes. *Ambio*, *40*(6), 558-565. https://doi.org/10.1007/s13280-011-0163-3

Lantmäteriet. (n.d.). *RTK*. Lantmäteriet. Retrieved 04/04 from https://www.lantmateriet.se/sv/Kartor-och-geografisk-information/gps-geodesi-och-swepos/GPS-och-satellitpositionering/Metoder-for-GNSS-matning/RTK/

Luoto, M., & Seppälä, M. (2003). Thermokarst ponds as indicators of the former distribution of palsas in Finnish Lapland. *Permafrost and periglacial processes*, *14*(1), 19-27.

Mamet, S. D., Chun, K. P., Kershaw, G. G., Loranty, M. M., & Peter Kershaw, G. (2017). Recent increases in permafrost thaw rates and areal loss of palsas in the Western Northwest Territories, Canada. *Permafrost and periglacial processes*, *28*(4), 619-633.

Massonnet, D., & Feigl, K. L. (1998). Radar interferometry and its application to changes in the Earth's surface. *Reviews of geophysics*, *36*(4), 441-500.

McKenzie, J. M., & Voss, C. I. (2013). Permafrost thaw in a nested groundwater-flow system. *Hydrogeology Journal*, *21*(1), 299-316.

Meyer, F. (2019). Spaceborne Synthetic Aperture Radar: Principles, data access, and basic processing techniques. In *Synthetic Aperture Radar (SAR) Handbook: Comprehensive Methodologies for Forest Monitoring and Biomass Estimation* (pp. 21-64).

Mohammadimanesh, F., Salehi, B., Mahdianpari, M., English, J., Chamberland, J., & Alasset, P.-J. (2019). Monitoring surface changes in discontinuous permafrost terrain using small baseline SAR interferometry, object-based classification, and geological features: a case study from Mayo, Yukon Territory, Canada. *GIScience & Remote Sensing*, *56*(4), 485-510. https://doi.org/10.1080/15481603.2018.1513444

Olvmo, M., Holmer, B., Thorsson, S., Reese, H., & Lindberg, F. (2020). Sub-arctic palsa degradation and the role of climatic drivers in the largest coherent palsa mire complex in Sweden (Vissátvuopmi), 1955–2016. *Scientific Reports*, *10*(1), 8937. https://doi.org/10.1038/s41598-020-65719-1

Philipp, M., Dietz, A., Buchelt, S., & Kuenzer, C. (2021). Trends in Satellite Earth Observation for Permafrost Related Analyses—A Review. *Remote Sensing*, *13*(6), 1217. https://www.mdpi.com/2072-4292/13/6/1217

Plaza, C., Pegoraro, E., Bracho, R., Celis, G., Crummer, K. G., Hutchings, J. A., Hicks Pries, C. E., Mauritz, M., Natali, S. M., & Salmon, V. G. (2019). Direct observation of permafrost degradation and rapid soil carbon loss in tundra. *Nature Geoscience*, *12*(8), 627-631.

Rizzoli, P., Martone, M., Gonzalez, C., Wecklich, C., Borla Tridon, D., Bräutigam, B., Bachmann, M., Schulze, D., Fritz, T., Huber, M., Wessel, B., Krieger, G., Zink, M., & Moreira, A. (2017). Generation and performance assessment of the global TanDEM-X digital elevation model. *ISPRS Journal of Photogrammetry and Remote Sensing*, *132*, 119-139. https://doi.org/https://doi.org/10.1016/j.isprsjprs.2017.08.008

Rosen, P. A., Hensley, S., Joughin, I. R., Li, F. K., Madsen, S. N., Rodriguez, E., & Goldstein, R. M. (2000). Synthetic aperture radar interferometry. *Proceedings of the IEEE*, *88*(3), 333-382.

Rudy, A. C. A., Lamoureux, S. F., Treitz, P., Short, N., & Brisco, B. (2018). Seasonal and multi-year surface displacements measured by DInSAR in a High Arctic permafrost environment [Article]. *International Journal of Applied Earth Observation and Geoinformation*, *64*, 51-61. https://doi.org/10.1016/j.jag.2017.09.002

Sannel, A. B. K., Hugelius, G., Jansson, P., & Kuhry, P. (2016). Permafrost warming in a subarctic peatland–which meteorological controls are most important? *Permafrost and periglacial processes*, *27*(2), 177-188.

Schuur, E. A. G., McGuire, A. D., Schädel, C., Grosse, G., Harden, J. W., Hayes, D. J., Hugelius, G., Koven, C. D., Kuhry, P., Lawrence, D. M., Natali, S. M., Olefeldt, D., Romanovsky, V. E., Schaefer, K., Turetsky, M. R., Treat, C. C., & Vonk, J. E. (2015). Climate change and the permafrost carbon feedback. *Nature*, *520*(7546), 171-179. https://doi.org/10.1038/nature14338

Seppälä, M. (2003). Surface abrasion of palsas by wind action in Finnish Lapland. *Geomorphology*, *52*(1-2), 141-148.

Short, N., LeBlanc, A.-M., Sladen, W., Oldenborger, G., Mathon-Dufour, V., & Brisco, B. (2014). RADARSAT-2 D-InSAR for ground displacement in permafrost terrain, validation from Iqaluit Airport, Baffin Island, Canada. *Remote Sensing of Environment*, *141*, 40-51. https://doi.org/https://doi.org/10.1016/j.rse.2013.10.016

Sjöberg, Y., Marklund, P., Pettersson, R., & Lyon, S. W. (2015). Geophysical mapping of palsa peatland permafrost. *The Cryosphere*, *9*(2), 465-478. https://doi.org/10.5194/tc-9-465-2015

Sollid, J. L., & Sørbel, L. (1998). Palsa Bogs as a Climate Indicator: Examples from Dovrefjell, Southern Norway. *Ambio*, *27*(4), 287-291. http://www.jstor.org.ezproxy.ub.gu.se/stable/4314737

Sowter, A., Bateson, L., Strange, P., Ambrose, K., & Syafiudin, M. F. (2013). DInSAR estimation of land motion using intermittent coherence with application to the South Derbyshire and Leicestershire coalfields. *Remote Sensing Letters*, *4*(10), 979-987.

Tarnocai, C., Canadell, J. G., Schuur, E. A. G., Kuhry, P., Mazhitova, G., & Zimov, S. (2009). Soil organic carbon pools in the northern circumpolar permafrost region. *Global Biogeochemical Cycles*, *23*(2). https://doi.org/https://doi.org/10.1029/2008GB003327

Wang, L., Marzahn, P., Bernier, M., & Ludwig, R. (2020). Sentinel-1 InSAR measurements of deformation over discontinuous permafrost terrain, Northern Quebec, Canada. *Remote Sensing of Environment*, *248*, 111965. https://doi.org/https://doi.org/10.1016/j.rse.2020.111965

Westermann, S., Duguay, C. R., Grosse, G., & Kääb, A. (2015). 13 Remote sensing of permafrost and frozen ground.

Yang, M., Nelson, F. E., Shiklomanov, N. I., Guo, D., & Wan, G. (2010). Permafrost degradation and its environmental effects on the Tibetan Plateau: A review of recent research. *Earth-Science Reviews*, *103*(1), 31-44. https://doi.org/https://doi.org/10.1016/j.earscirev.2010.07.002

Zuidhoff. (2002). Recent decay of a single palsa in relation to weather conditions between 1996 and 2000 in Laivadalen, northern Sweden. *Geografiska annaler. Series A, Physical geography*, *84*(2), 103-111. https://doi.org/10.1111/j.0435-3676.2002.00164.x

Zuidhoff, & Kolstrup. (2000). Changes in palsa distribution in relation to climate change in Laivadalen, northern Sweden, especially 1960–1997. *Permafrost and periglacial processes*, *11*(1), 55-69.

Zwieback, S., Liu, X., Antonova, S., Heim, B., Bartsch, A., Boike, J., & Hajnsek, I. (2016). A Statistical Test of Phase Closure to Detect Influences on DInSAR Deformation Estimates Besides Displacements and Decorrelation Noise: Two Case Studies in High-Latitude Regions. *IEEE Transactions on Geoscience and Remote Sensing*, *54*(9), 5588-5601. https://doi.org/10.1109/TGRS.2016.2569435

Åkerman, H. J., & Johansson, M. (2008). Thawing permafrost and thicker active layers in sub-arctic Sweden. *Permafrost and periglacial processes*, *19*(3), 279-292.